Article:
Liu, B., He, S., Moulinec, C. et al. (2022) A multiscale model of a rod bundle using subchannel CFD. Nuclear Engineering and Design, 393. 111793. ISSN: 0029-5493

https://doi.org/10.1016/j.nucengdes.2022.111793

Nuclear Engineering and Design 393 (2022) 111793

Contents lists available at ScienceDirect

Nuclear Engineering and Design

journal homepage: www.elsevier.com/locate/nucengdes

A multiscale model of a rod bundle using subchannel CFD

B. Liu [a,*], S. He [a], C. Moulinec [b], J. Uribe [c]

[a] Department of Mechanical Engineering, University of Sheffield, Sheffield S1 3JD, UK
[b] Science and Technology Facilities Council Scientific Computing Department, Daresbury Laboratory, Warrington WA4 4AD, UK
[c] EDF Energy R&D UK Centre, Manchester M13 9PL, UK

ARTICLE INFO

Keywords:
Computational fluid dynamics
Coarse mesh
Coupling
Porous media
Rod bundle
Multiscale

ABSTRACT

This paper deals with a coarse-mesh Computational Fluid Dynamics (CFD) approach, referred to as Subchannel CFD (SubChCFD), which combines features of the traditional 1-D subchannel analysis tools used in nuclear thermal hydraulic analyses and modern CFD. The SubChCFD, which has been previously developed for flow simulations, has been extended to perform thermal simulations and is then applied to a complex nuclear fuel bundle to explore and demonstrate the capacity of this new tool. SubChCFD allows resolved CFD sub-models to be nested into the regions that are of interest to locally improve the prediction, and can be coupled with the porous media approach to deal with any sub-scale fine structures that are difficult to be handled using a coarse mesh.

In the present case studied, a SubChCFD baseline model is created, covering the entire heated length of the test geometry, to capture the axial developments of the flow and heat transfer in the rod bundle. Spacer grids that are used to keep the rods in place are modelled as embedded porous media to account for the associated blockage effect and pressure losses. In addition, a resolved CFD sub-model is created and coupled with the baseline model to improve the prediction for the region where high fidelity experimental measurements were performed. Through the present test, SubChCFD shows good predictability, flexibility and scalability in modelling large nuclear reactor components with complex internal structures. With the advanced coupling functionality, it is able to produce comparable simulation results to that of conventional CFD methods for regions of interest, with greatly reduced computational cost.

1. Introduction

Unresolved, coarse-mesh Computational Fluid Dynamics (CFD) approaches have been increasingly recognised as a promising solution for 3-D Thermal Hydraulic (T/H) analysis of large-scale reactor structures in nuclear systems, such as fuel assemblies or the entire reactor core. These structures normally contain hundreds of thousands of flow channels, resulting in numerous length scales of the flow therein, and are difficult to be handled using resolved CFD due to the high demand in computing resources. In a typical coarse-mesh CFD approach, the computing cost is reduced by using a low resolution mesh, but the simulation accuracy can still be retained to a desired degree depending on the specific purpose of the calculation and modelling techniques used. One of the main advantages of the coarse-mesh CFD approaches over the traditional 1-D subchannel analysis tools is their CFD-like capability which allows it to resolve some key 3-D flow phenomena that are valuable to reactor designers in making early decisions and/or reactor engineers in carrying out safety assessments of the reactors.

In the past decade, multiple coarse-mesh CFD approaches have been developed to achieve different levels of reduction in modelling resolution. Hu and Fanning (2013) developed a momentum source term model to mimic the effects of the wire-wrap spacers in a wire-wrapped rod bundle without the need to fully resolve the geometrical details of the wires using fine meshes. Roelofs et al. (2012) and Roelofs and Doolaard (2017) proposed a so-called reduced resolution method in which the mesh is carefully coarsened by mainly neglecting the offset layers near physical walls. The method was proved to produce results at an accuracy comparable to the well resolved simulations, but the mesh used is up to 10 time smaller than the latter. Despite encouraging performances observed, the reduction in mesh resolution in the aforementioned methods is limited, as they still rely on the same near-wall modelling techniques as conventional CFD does (i.e. wall function approaches), so they are still likely to be too computationally expensive for real size fuel assemblies. To further reduce the computing cost, Viellieber and Class

* Corresponding author.
E-mail address: bo.liu@sheffield.ac.uk (B. Liu).

https://doi.org/10.1016/j.nucengdes.2022.111793
Received 29 April 2021; Received in revised form 23 February 2022; Accepted 23 April 2022
Available online 2 May 2022

Table 1
Summary of representative coarse-mesh CFD approaches for nuclear T/H applications.

Methods	Fuel rods	Spacers and other sub-scale structures	Closure modelling for near-wall effects	Mesh resolution
Momentum source term (Hu and Fanning, 2013)	Resolved	Implicitly resolved	Wall functions & momentum source	Medium
Reduced resolution CFD (Roelofs et al., 2012; Roelofs and Doolaard, 2017)	Resolved	Resolved	Wall functions	Medium low
Low resolution CFD (Mikuž and Roelofs, 2020)	Resolved	Porous media	Wall functions	Low
CG-CFD (Class et al., 2011; Viellieber and Class, 2012)	Resolved	Porous media	Data from resolved CFD	Low
SubChCFD (Liu et al., 2021a, 2021b, 2019)	Resolved	Porous media	Empirical (subchannel) correlations	Low
3-D subchannel codes (Yoon et al., 2017; Gerschenfeld et al., 2019)	Porous media	Porous media	Empirical (subchannel) correlations	Very low
Porous media CFD (Fiorina et al., 2015; Yu et al., 2015)	Porous media	Porous media	Empirical correlations	Very low

(2012) employed a much coarser mesh in their so-called Coarse-Grid CFD (CG-CFD) approach where the fuel rods are explicitly resolved and the spacers are represented using porous media. Instead of solving a full set of Navier-Stokes equations, the Euler equations were solved with diffusion effects accounted for using a volumetric force extracted from the resolved CFD simulations pre-performed on the same geometry. As opposed to Viellieber and Class, Hanna et al. (2020) employed a surrogate statistical model to offset the numerical errors arising from grid coarsening using the state-of-the-art machine learning technology. However, the large amount of data required to train the surrogate model are still provided using resolved CFD simulations. Another line to obtain a coarse-mesh CFD model is based on the porous media approach, in which most of the solid structures, including the fuel rods and spacers, are modelled using porous media and the pressure drop and sub-scale heat transfer are accounted for using empirical correlations. Such approaches include, for example, the multi-scale multi-physics reactor analysis tool GeN-Foam (Fiorina et al., 2015), CEA's T/H analysis tool PolyMAC (Gerschenfeld et al., 2019) and KAERI's 3-D subchannel code CUPID (Yoon et al., 2017).

In our recent work (Liu et al., 2019), a coarse-mesh CFD approach was developed based on a hybrid technique combining the features of the traditional subchannel tools used for nuclear T/H analyses and modern CFD. The new method is referred to as Subchannel CFD (SubChCFD) in which the main geometry of the subchannel structures is resolved similarly as that in the methods of Viellieber and Class (2012) and Mikuž and Roelofs (2020) using a very coarse mesh, but differently, the wall effects are accounted for using well-validated industry-standard correlations that are usually used in traditional subchannel analysis codes. This ensures the method to provide results similar to the well-calibrated subchannel results for 'straight' fuel channels at nominal operating conditions. Later, new functionalities that allow SubChCFD to be coupled with resolved CFD (Liu et al., 2021a) and the porous media approaches (Liu et al., 2021b) were developed. This has enhanced the modelling capability of SubChCFD so that it can be used for a wider range of flow scenarios. The coupling between SubChCFD and resolved CFD is achieved using a novel domain overlapping technique, which allows greater details of the flow to be resolved in the regions of interest without a significant modification to the mathematical system of SubChCFD, making the coupling extremely flexible. Coupling SubChCFD with the porous media approach is somewhat more straightforward and can be achieved using the so-called model 'embedding' or 'interfacing' depending on the specific scenarios being dealt with. This enables SubChCFD to handle some complex sub-scale structures that are difficult to be resolved using a coarse mesh and ensures reliable predictions for some large-scale flow structures and/or the overall T/H behaviours of the system. Table 1 shows a summary of some representative coarse-mesh CFD approaches that are currently available for nuclear T/H analyses.

The main purpose of this paper is to develop and test heat transfer capabilities of SubChCFD and demonstrate the new tool within complex industrial applications. In addition, the coupling capabilities that have been validated separately using multiple test cases in our previously published work (Liu et al., 2021a, 2021b) will be tested simultaneously in a single simulation to evaluate the uncertainties and overall performance of the code and the compatibility between the different sub-model coupling options. The combination of the various functionalities of the complete SubChCFD tool together will offer considerable benefit in practice. For example, a well-developed SubChCFD model for a nuclear reactor core structure would use porous media model to approximate complex repetitive structures and resolved CFD sub-models to capture the T/H details of the flow in regions of particular interest.

The case to be studied in this paper is one of the New Experimental Studies of Thermal-Hydraulics of Rod Bundles (NESTOR) series of experiments (Wells et al., 2015) in which the test facility used closely resembles a real-world Pressurised Water-cooled Reactor (PWR) fuel bundle and the pressure and temperature cover the normal PWR operating conditions. The experiments provide a variety of high-fidelity measured data, including axial mean velocity distribution, Root Mean Square (RMS) velocity fluctuation, pressure drop and rod wall surface temperature, etc., which are useful detailed data for the validation of numerical simulations. In addition, the EPRI's CFD Round Robin benchmark exercise (EPRI, 2015, 2014) based on the NESTOR experiments have attracted participants from various organisations who have provided abundant CFD simulation results that can be used for cross-code comparison with the current simulation to further evaluate the strengths and drawbacks of the new method against conventional CFD tools.

The NESTOR experiments were conducted in two different test loop facilities – the isothermal MANIVEL and the thermal OMEGA facilities. A case from the latter is used in this paper, though some measurements from a MANIVEL test were also used for comparison as described in the Section 4. The test section of each facility consists of two types of 5×5 rod bundles: the Simple Support Grid (SSG) bundle and the Mixing Vane Grid (MVG) bundle. The two types of rod bundles are very similar in configuration with the main difference lying in the spacer grids installed. All spacer grids installed in the SSG bundle are SSGs, while SSGs and MVGs are installed alternatingly in the MVG bundle. Both types of the spacer grids are expected to have significant effects on the T/H behaviours of the downstream coolant flow in the rod bundle and should be taken into account carefully in the numerical modelling. In SubChCFD, the spacer grids can be either modelled using the porous media approach for the purpose of capturing the global effects, such as flow blockage and pressure drop, or represented explicitly through coupling with resolved CFD for the purpose of resolving the details of the flow in important regions. In this paper, both of the coupling approaches are used. First, a SubChCFD baseline model is created based on the bare bundle geometry, then the spacer grids are described using embedded porous media, so that the mesh is simple and consistent across the entire domain. Finally, a resolved CFD sub-model is created to cover the most interested grid span, that is, the so-called target span where experimental measurements were performed, to capture the detailed flow and

temperature field.

The SSG bundle is selected for the numerical test considering the simplicity of meshing for the SSG in the resolved sub-model. Nevertheless, the associated modelling strategy used and conclusions drawn for the numerical assessments also apply to the MVG bundle case.

The following shows an outline of this paper. In Section 2, the methodologies of the baseline SubChCFD and the coupling functionalities developed in our previous work are outlined briefly. The test case studied and the associated experimental facility used are described in Section 3 along with a detailed description of the modelling strategy, mesh system and some additional developments to improve the coupled simulation. Results are presented and analysed in Section 4. They are compared with the experimental data as well as the CFD simulations of the Round Robin benchmarking exercise for validation and evaluation of the coupled model system. Conclusions are drawn in Section 5.

2. Outline of the SubChCFD methodology

2.1. The baseline SubChCFD

As explained in the introduction, SubChCFD adopts a hybrid technique combining the features of the traditional subchannel analysis tools and modern CFD, in which a dual mesh system is used, including, namely, (i) a subchannel filtering mesh which aligns with the mesh used in typical subchannel codes, enabling the subchannel-level wall friction and heat transfer calculated using existing engineering correlations, and (ii) a computing mesh, on which a full set of 3-D Reynolds Average Navier-Stokes (RANS) governing equations are solved with a near-wall closure method based on calculations of step (i). The computing mesh is much finer than the subchannel mesh but is still very coarse in CFD standard. The friction and heat transfer obtained from the subchannel calculation are used in the CFD via boundary conditions to ensure that the integral effect of the flow solution is consistent with existing engineering correlations. On the other hand, the CFD results are integrated over the subchannel mesh to produce the integral flow parameters (e.g. velocity, thermal properties), which are used in the subchannel calculations. Details of the development, implementation and validation of the baseline SubChCFD were reported in Liu et al. (2019). A brief summary of the method is presented below.

First, the incompressible RANS continuity and momentum equations are recalled as follows,

$$\nabla\cdot\vec{u}=0 \tag{1}$$

$$\rho\frac{\partial\vec{u}}{\partial t}+\rho\nabla\cdot(\vec{u}\otimes\vec{u})=-\nabla p+\nabla\cdot\bar{\bar{\sigma}}+\vec{S}_M \tag{2}$$

where $\vec{u}$ is the velocity vector, ρ is fluid density, t is time, p is pressure, $\bar{\bar{\sigma}}$ is the stress tensor including both the viscous and the turbulence contributions, $\vec{S}_M$ is the body force. The computing mesh-based Finite Volume (FV) integration of the RANS momentum equation (Eq. (2)) with a collocated arrangement of the velocity components can be written as follows,

$$\frac{\rho V_\Omega}{\Delta t}(\vec{u}^{n+1}-\vec{u}^{n})+\oint_S\vec{u}^{n+1}\left(\vec{J}^{n}\cdot\vec{n}\right)dS = -\oint_S(\bar{\bar{I}}p\cdot\vec{n})dS+\oint_S\left(\bar{\bar{\sigma}}^{n+1}\cdot n\right)dS+V_\Omega S_M^n \tag{3}$$

where V_Ω is the volume of the computing mesh cellΩ, Δt is the time step size, superscript n and $n+1$ represent the nth and the (n + 1)th time step, respectively, $\vec{J}=\rho\vec{u}$ represents the convective mass flux, $\vec{n}$ is the unit normal vector of the cell surface, S is the area of the cell surface, $\bar{\bar{I}}$ is the unit tensor. To implement SubChCFD, the diffusion term of Eq. (3) is further decomposed into an interior part and a wall boundary part:

$$\oint_S\bar{\bar{\sigma}}\cdot\vec{n}\,dS=\underbrace{\int_{S_f}\bar{\bar{\sigma}}\cdot\vec{n}\,dS}_{interior}+\underbrace{\int_{S_w}\bar{\bar{\sigma}}\cdot\vec{n}\,dS}_{\text{wall boundary}} \tag{4}$$

where the interior part is modelled no differently from a standard eddy viscosity RANS approach and can be written as follows,

$$\int_{S_f}\bar{\bar{\sigma}}\cdot\vec{n}\,dS=\int_{S_f}(\mu+\mu_t)\left[\nabla\vec{u}+(\nabla\vec{u})^{\mathrm{T}}-\frac{2}{3}\delta\nabla\cdot\vec{\mathbf{u}}\right]\cdot\vec{n}\,dS \tag{5}$$

where μ is the dynamic viscosity of the fluid, μ_t is the eddy viscosity which is modelled using appropriate first order moment closure turbulence models. The wall boundary part, however, is modelled as a whole using the following expression,

$$\int_{S_w}\bar{\bar{\sigma}}\cdot\vec{n}\,dS=-\frac{1}{4}f\frac{1}{2}\rho_{SC}\vec{u}_{SC}|\vec{u}_{SC}|\int_{S_w}dS \tag{6}$$

where f denotes the Darcy frictional factor calculated using relevant subchannel friction correlations, depending on the specific configurations of the fuel assembly simulated, ρ_{SC} and $\vec{u}_{SC}$ are the subchannel bulk density and bulk velocity, respectively, derived by averaging the CFD solutions over the corresponding filtering mesh cells.

SubChCFD is currently implemented in and validated for an open-source FV CFD package Code_Saturne (Fournier et al., 2011). However, it is possible to implement it in other CFD platforms.

2.2. Coupling with embedded porous media sub-models

SubChCFD can be coupled with embedded porous media models to account for any sub-scale fine structures that are not suitable to be resolved using a coarse mesh. In such an approach, a computational domain with an explicit representation of the main subchannel geometry is still used. Flow regions with sub-scale fine structures are considered as porous media. A spatial averaging operator is then applied to the RANS governing equations (Eqs. (1) and (2)) over the porous media regions to obtain the macroscopic equations, which reads as follows,

$$\nabla\cdot(\gamma_V\langle\vec{u}\rangle)=0 \tag{7}$$

$$\rho\frac{\partial(\gamma_V\langle\vec{u}\rangle)}{\partial t}+\rho\nabla\cdot(\gamma_V\langle\vec{u}\rangle\otimes\langle\vec{u}\rangle)=-\gamma_V\nabla\langle p\rangle+\nabla\cdot(\gamma_V\langle\bar{\bar{\sigma}}\rangle)+\gamma_V\left\langle\vec{S}_M\right\rangle+\gamma_V\vec{R} \tag{8}$$

where γ_V is the volume porosity, representing the ratio of the volume occupied by the fluid and the total volume of the averaging operator:

$$\gamma_V=\frac{V_f}{V} \tag{9}$$

$\vec{R}$ is an unknown momentum source term that appears due to spatial averaging, accounting for the resistance forces exerted by the sub-scale fine structures on the fluid. A closure modelling is required to determine this term by relating it to the local macroscopic flow quantities. Symbols within the angle bracket represent the intrinsic average of the corresponding fluid quantities. The intrinsic average of a variable ϕ is defined as follows,

$$\langle\phi\rangle=\frac{1}{V_f}\int_{V_f}\phi dV \tag{10}$$

It can be observed that the macroscopic governing equations (Eqs. (7) and (8)) for the porous media regions closely resemble the RANS equations (Eqs. (1) and (2)) for the rest of the domain, although the physical meaning of the unknowns are different. Solution of the obtained equation system can be simply organised into a single CFD instance with switchable equation coefficients among different regions.

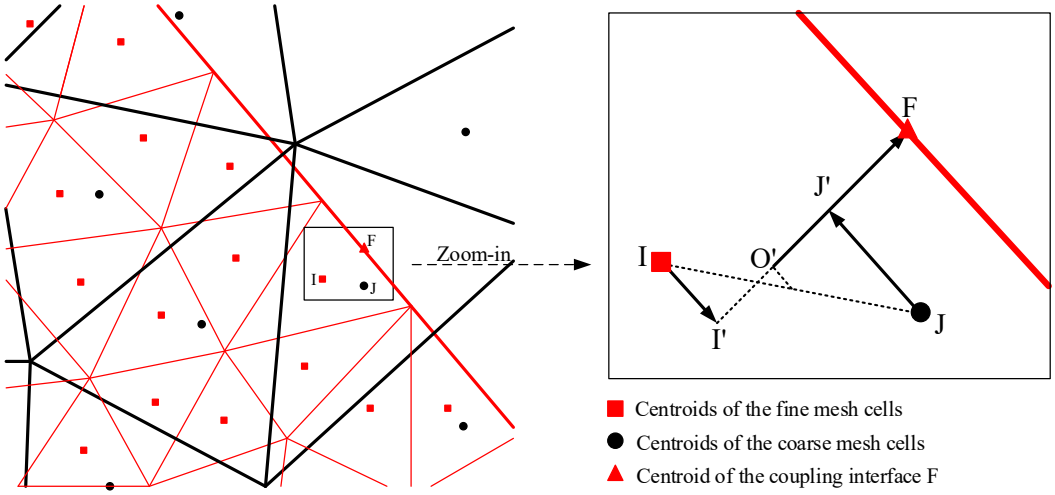

Fig. 1. Calculation of the interface velocity.

Similar to that in the baseline SubChCFD, the FV integration is performed over the coarse-grid computing mesh that covers the entire domain to discretise the equations and the near-wall SubChCFD treatment (Eqs. (4)–(6)) is then applied for a near-wall closure modelling. Details about the implementation and validation of the coupling between SubChCFD and the porous media approach can be found in Liu et al. (2021b).

2.3. Domain overlapping coupling with resolved CFD sub-models

SubChCFD allows resolved CFD sub-models to be nested into the regions that are of interest to locally improve the prediction. Such a coupling is achieved using a domain-overlapping approach in which the resolved fine-mesh model receives data from the coarse-mesh solution to define its boundary conditions for the coupling interfaces. A Dirichlet-type boundary condition is used for velocity, and accordingly, a homogeneous Neumann condition is used for pressure. Fig. 1 shows a schematic that illustrates how the interface velocity is calculated in a coupled mesh system. As can be seen, the interface velocity at target face centre F in the fine mesh is calculated using the velocities at cell centre I (the cell adjacent to face F in the fine mesh) and J (the cell closest to I in the coarse mesh), respectively. The two velocities are then projected

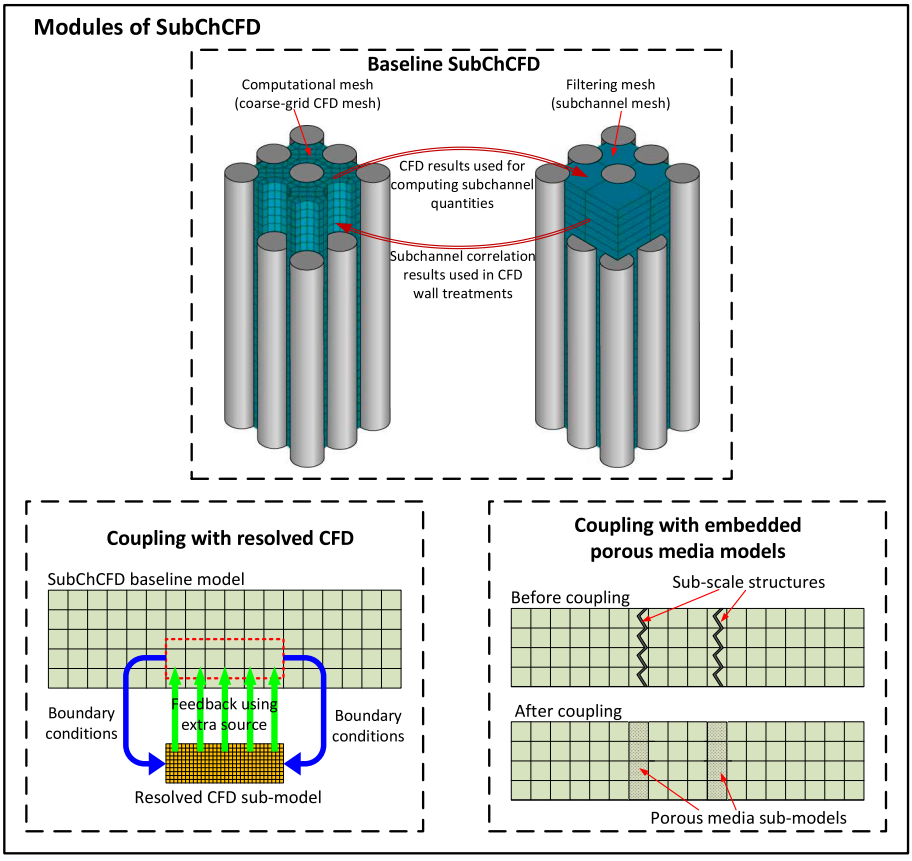

Fig. 2. Outline of the SubChCFD methodology.

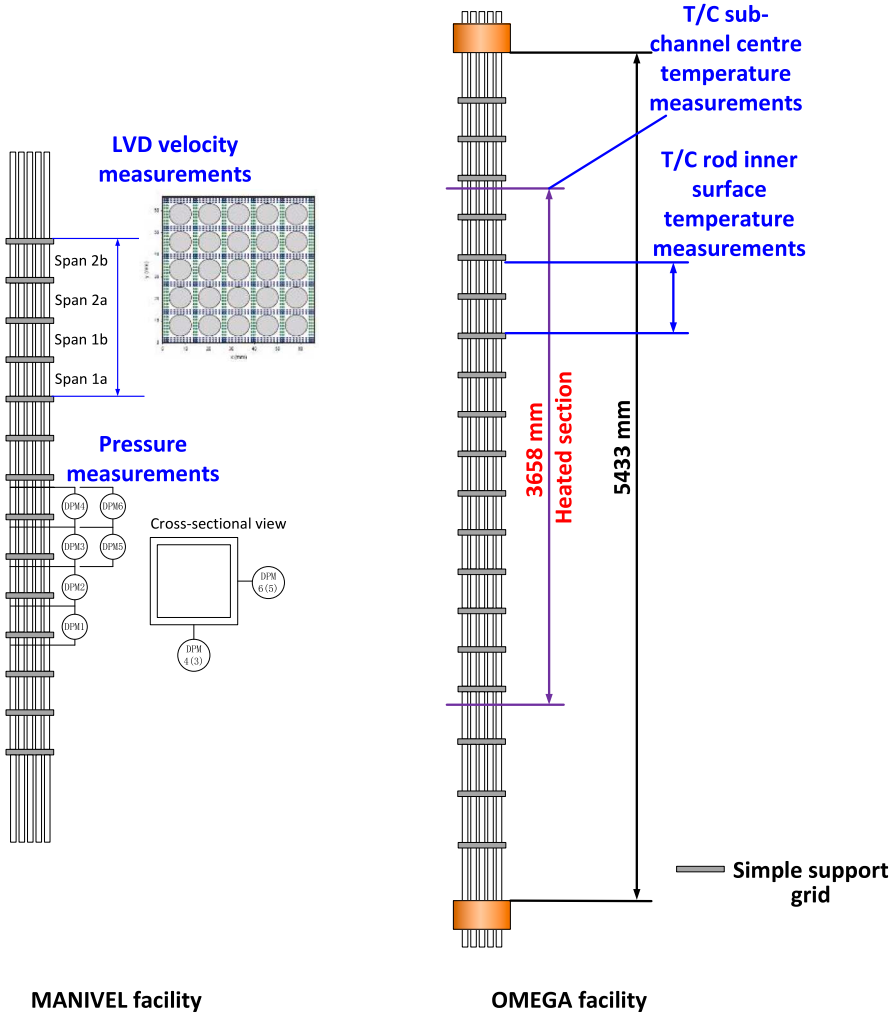

Fig. 3. Test sections and measurement information in the NESTOR experiment.

onto the orthogonal line I'J' to face F at locations with equal distance to point F. Then, the interface velocity $\vec{u}_F$ is calculated as an equal-weighted blending of them using the following equation,

$$\vec{u}_F = 0.5\left[\vec{u}_J + \nabla\vec{u}_J\cdot\left(\overrightarrow{JJ'} + \overrightarrow{O'F}\right)\right] + 0.5\left[\vec{u}_I + \nabla\vec{u}_I\cdot\left(\overrightarrow{II'} + \overrightarrow{O'F}\right)\right] \tag{11}$$

The advantage of such a treatment over using information just from the coarse mesh to calculate the interface quantities is to improve the numerical stability of the coupling.

Feedback is also allowed from the resolved fine-mesh model to the coarse-mesh SubChCFD model to locally improve the predictions of the latter. This two-way coupling is achieved by adding an additional momentum source term to the coarse-mesh equation as a penalty to force the velocity solution to approach that of the resolved fine-mesh model. The momentum source is based on the local velocity difference between the two meshes and can be formulated as follows,

$$\vec{S}^n_\Delta = \eta\frac{\rho^n}{\Delta t}(\vec{u}^n_{dis} - \vec{u}^n_{loc}) \tag{12}$$

where $\vec{u}^n_{loc}$ is the cell centre velocity of the 'local' coarse mesh, u^n_{dis} is the velocity of the 'distant' fine mesh interpolated from the closest cell centre to the location where u^n_{loc} is stored, η is a user prescribed correction factor, representing to what extent the coarse-mesh result is expected to be corrected by that of the resolved model. A more detailed description of the coupling between SubChCFD and resolved CFD sub-models can be found in Liu et al. (2021a).

Fig. 2 shows an outline of the SubChCFD methodology, including schematics of the baseline model as well as the coupling modules.

3. Subchannel CFD model of the 5 × 5 rod bundle

3.1. Facility and experimental measurements

The two test facilities used in the NESTOR experiment are depicted in Fig. 3. The rod bundles used in these facilities were very similar to one another in terms of rod diameter, pitch-to-diameter ratio and axial spacing of the spacer grids. The rod bundles consisted of a 5 × 5 square array of tube rods enclosed in a square bundle casing. The rod outer diameter was 9.50 ± 0.02 mm, and the array pitch and rod-to-wall gap were 12.6 mm and 3.1 mm, respectively. The resulted width of the bundle casing was 61.1 mm. The total length of the rod was approximately 5 m, including of a heated length of 3.658 m in the OMEGA experiment. The thickness of the tube used in the OMEGA bundle were different for the 9 inner rods and the 16 peripheral rods. They were 0.9 mm and 0.675 mm, respectively, resulting in an inner-to-peripheral rod power peaking factor of ~ 1.3. The tube rods used in the MANIVEL facility were made of 316L stainless steel, while the heater rods were made of Inconel 600 precision cold-drawn tubes in the OMEGA facility. Some key physical properties of Inconel 600 (used in some of the simulations) are given in Table 2.

The SSG and the MVG used in the MANIVEL and the OMEGA

Table 2
Some key physical properties of Inconel alloy 600.

Density (kg/m^3)	Thermal conductivity (W/m/s)	Specific heat (J/kg/K)
8470	14.9	444

facilities were identical. The SSGs were a small honeycomb type grid (8 mm high and 0.2 mm thick) and were distributed evenly at axial intervals of 279 mm in the SSG rod bundle. The structural details of the SSG are shown in Fig. 4. The MVG was representative of the commercial Westinghouse F17 × 17 V5H design. Details of the MVG are not provided here, as the MVG bundle was not actually used in this paper. Those who are interested in this can directly refer to the Round Robin CFD benchmark reports (EPRI, 2015, 2014) for more details.

The two facilities were all operated with single-phase water at steady state flow conditions. The isothermal MANIVEL facility was operated at atmospheric temperature and pressure, providing measurements for the axial velocity and pressure drop. Laser Doppler Velocimetry (LDV) was used to measure the cross-sectional distribution of the mean and RMS axial velocity at several successive axial elevations of the top four grid spans. The exact locations of these measuring elevations are shown in Fig. 4. For each cross-section, around 1,900 measuring points were used to produce high fidelity data sets. The grid span pressure drops were measured using eight pressure taps distributed at intervals of 279 mm on the two perpendicular casing walls.

The thermal OMEGA facility was operated at a high pressure of 15.6 MPa and high inlet temperatures ranging from 250.5 °C to 282.2 °C, which covers the normal PWR operation conditions. Measurements were performed for the subchannel centre fluid temperature and the rod wall inner-surface temperature of the heating tubes. As is shown in Fig. 3, the former was performed at the End of the Heated Length (EOHL) to produce a full cross-sectional temperature map at the EOHL of the rod bundle, while the latter was performed over the uppermost four grid spans for the 9 inner rods to collect detailed 2-D distributions of temperature over the inner surfaces of the heated rod walls at axial and circumferential increments of 35 mm and 20° for the SSG bundle, and 30 mm and 15° for the MVG bundle, respectively.

3.2. Test case selected for simulation

One of the thermal cases in the OMEGA experiment carried out within the SSG rod bundle test section is selected for the numerical modelling. The T/H conditions for this case are shown in Table 3. The inlet temperature and the outlet pressure are 250.5 °C and 15.6 MPa, respectively. The mass flux is 4,540 kg/m^2/s, corresponding to a cross-sectional average inlet velocity (w_0) of around 5.6 m/s. The resulting inlet Reynolds number based on the regular subchannel hydraulic diameter and w_0 is 489,350.

Table 3
T/H conditions of the selected NESTOR-OMEGA test case.

Outlet pressure (MPa)	Mass flux (kg/m^2/s)	Reynolds number	Inlet temperature (°C)
15.6	4,540	489,350	250.5
Inner rod power (kW/rod)	Peripheral rod power (kW/rod)	All rods power (kW)	Total heating power (kW)
94.812	73.902	2,035.7	2,046

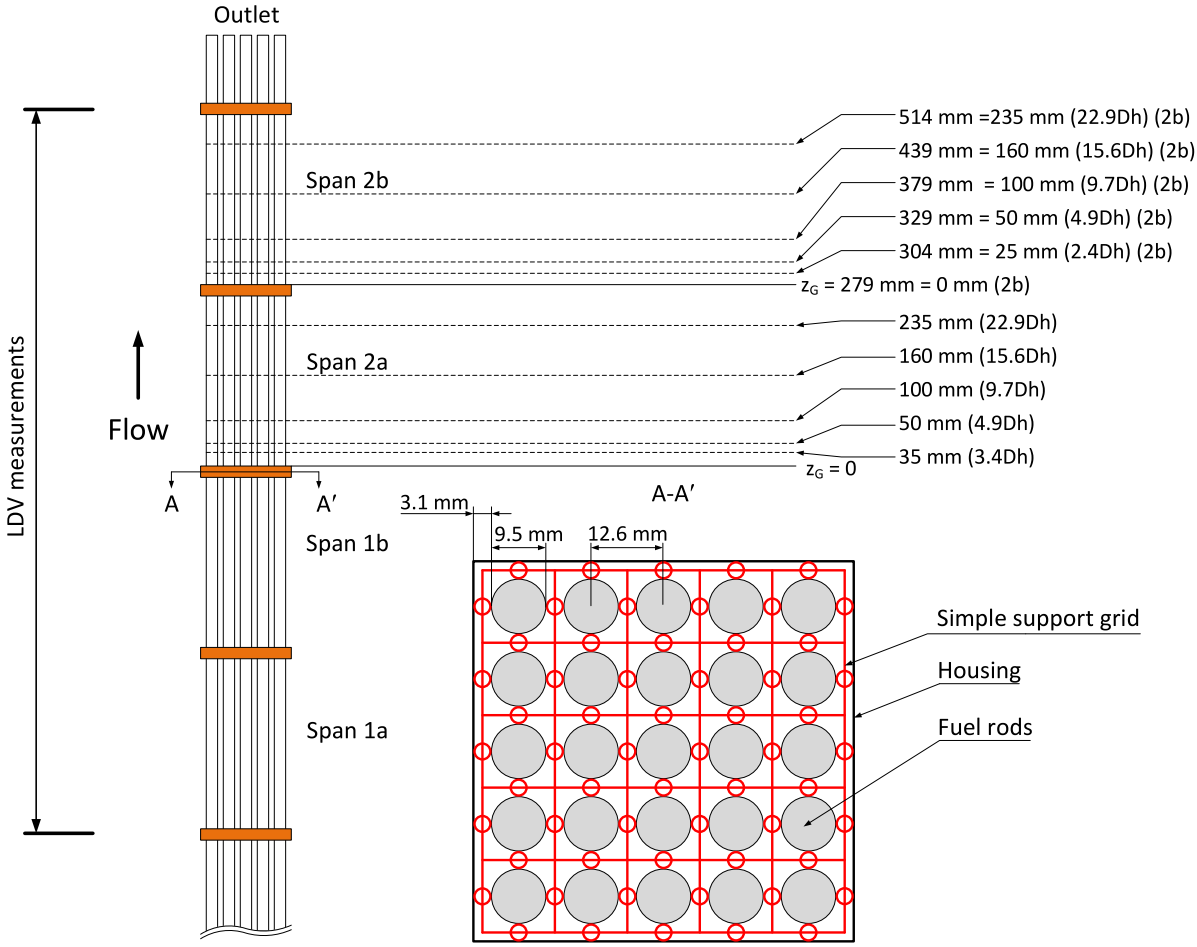

Fig. 4. Structural details of the SSG and the locations of LDV velocity measurements in the NESTOR MANIVEL experiment.

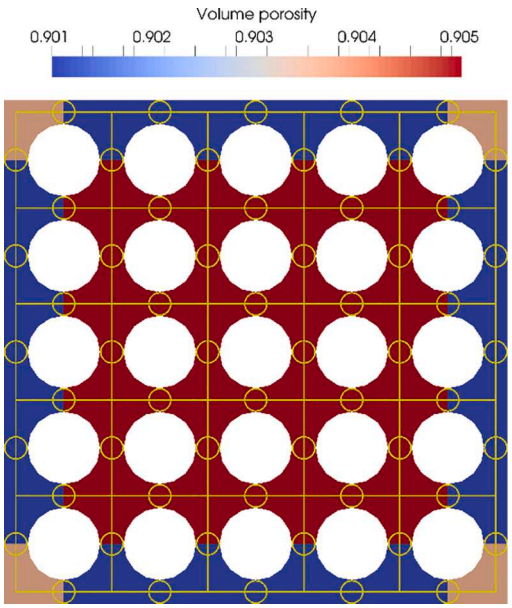

Fig. 5. Distribution of the volume porosity in the porous media sub-domains (The SSG is also shown).

The heating power of the inner 9 rods is higher than that of the 16 peripheral rods due to the larger thickness of the heating tube used. They are 94.812 kW/rod and 73.902 kW/rod, respectively, based on the Inconel 600 heated length without the copper connections, resulting in a heating power on all rods of 2035.7 kW. The total heating power given in the last column of Table 3 is slightly higher than this value, as it also includes consideration of the length of the copper connections.

3.3. Modelling strategy

With the rapid increase in computing power, nowerdays, numerical simulation of the full span of the SSG rod bundle using conventional CFD is possible but still at a high price. In the CFD Round Robin benchmarking exercise (EPRI, 2014), participants made various assumptions to reduce computing cost. For example, a quadrant domain was often used to replace the entire lateral domain taking the advantage of the geometrical symmetry. For the isothermal case (even some thermal cases), some participants only considered several spans in their simulations. They assumed that the flow in these spans has already fully developed and can be simulated using axial periodicity. Some participants divided the entire domain into several segments to reduce the demand in computing power. In this approach, numerical simulations were performed successively from the first to the last segment. Once the simulation was completed for an upstream segment, the converged flow and thermal fields at the outlet were mapped to the inlet of the adjacent segment downstream to obtain the boundary conditions for the latter. This approach enabled CFD simulations to be done for large domains like this with limited computer capability, but they may also result in extra uncertainties if used inappropriately.

3.3.1. The SubChCFD baseline model

Considering the fact that the flow and temperature information are accumulated over spans from the beginning of the heated section, a coarse-grid SubChCFD baseline model is created, covering the entire heated length, to capture the axial development of the flow. In addition, the computational domain is extended in both upstream and downstream directions to create two unheated sections at the inlet and the outlet, respectively. The unheated inlet section is 300 mm long (about $30D_h$), being used to implement a so-called mapped inlet method. That is, the velocity and scalars at a downstream location within this unheated domain is mapped to the inlet boundary to produce fully developed flow conditions before the heated section. The unheated outlet section is 100 mm long, being used merely to reduce the potential numerical effects of the outlet boundary conditions on the flow in the upstream heated section.

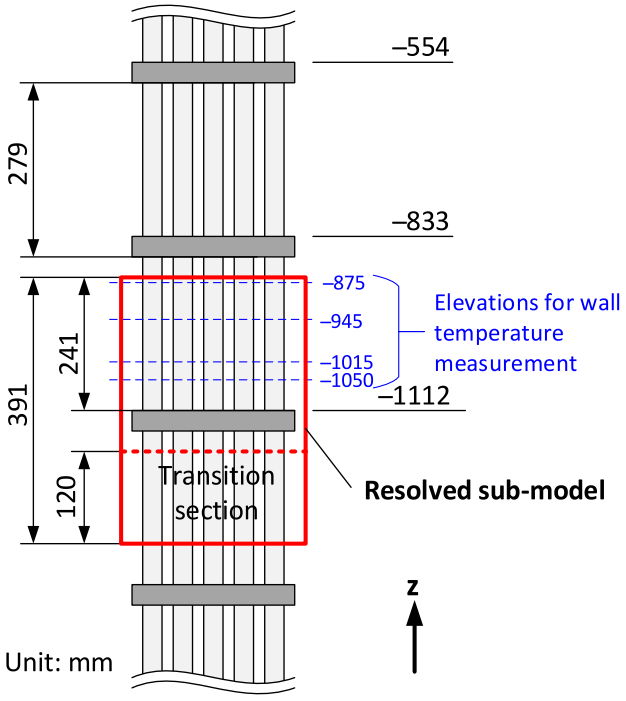

Fig. 6. Detailed dimensions of the resolved sub-model and axial (i.e. the z direction) elevations of the experimental measurements.

3.3.2. Coupling with embedded porous media

There are 13 SSGs distributed over the entire heated length and they are modelled as embedded porous media within the baseline model, so no explicit modifications are required to the coarse-grid mesh across these porous media sub-domains. The volume porosity is calculated based on subchannels and its spatial distribution is the same for the spacer regions of different spans. Fig. 5 shows a cross-sectional view of the volume porosity distribution in the porous media sub-domains.

The spacer-related pressure loss of the SSG is calculated using the following equation,

$$\Delta P_G = -\frac{1}{2}\rho_{ref} K_G \left(w_{ref} \cdot |w_{ref}|\right) \tag{13}$$

where K_G is the one-grid-span spacer-related pressure loss coefficient, taking the value of 0.42 in the present study (Rehme, 1973). More details of the implementation of the embedded porous media method in SubChCFD can be found in Liu et al. (2021b).

3.3.3. Coupling with resolved CFD sub-model

The simulation is refined for a target span using a resolved sub-model, which is coupled with the coarse-grid baseline model. According to Liu et al. (2021a), one of the key factors that can affect the performance of the coupling between SubChCFD and resolved CFD is the size and location of the computational domain used for the resolved sub-model. Normally, a relatively large domain should be used to avoid the coupling interfaces being placed too close to the regions of interest, so that the errors in boundary conditions obtained using the coarse-mesh results can be safely neglected. Fig. 6 shows the exact location as well as some key dimensions of the resolved sub-model. The main part of the

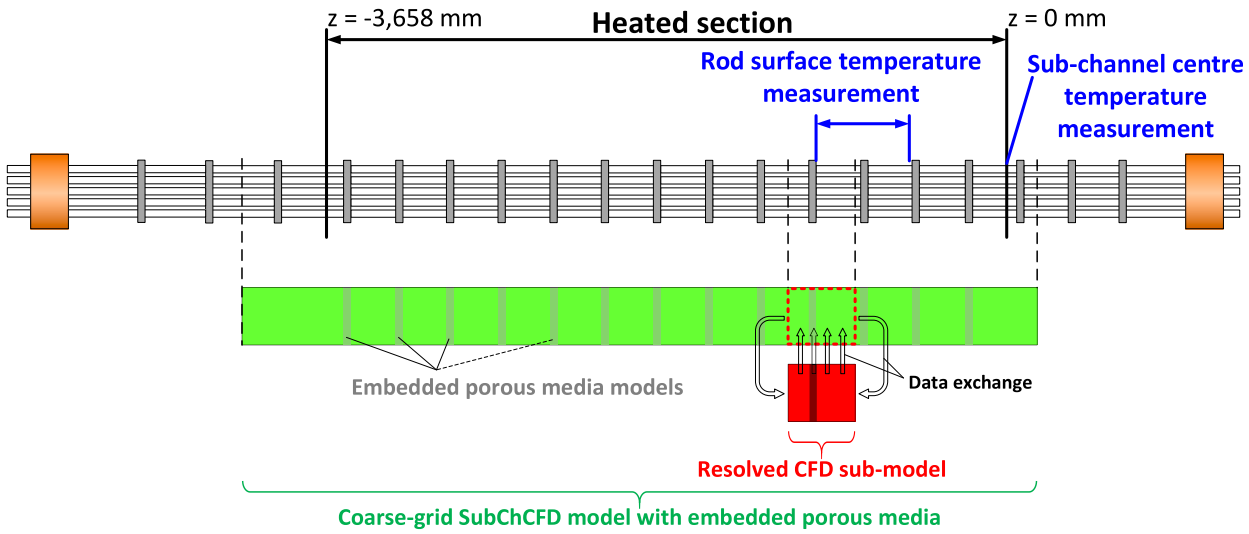

Fig. 7. Spatial arrangement of the computational domains in the coupling system.

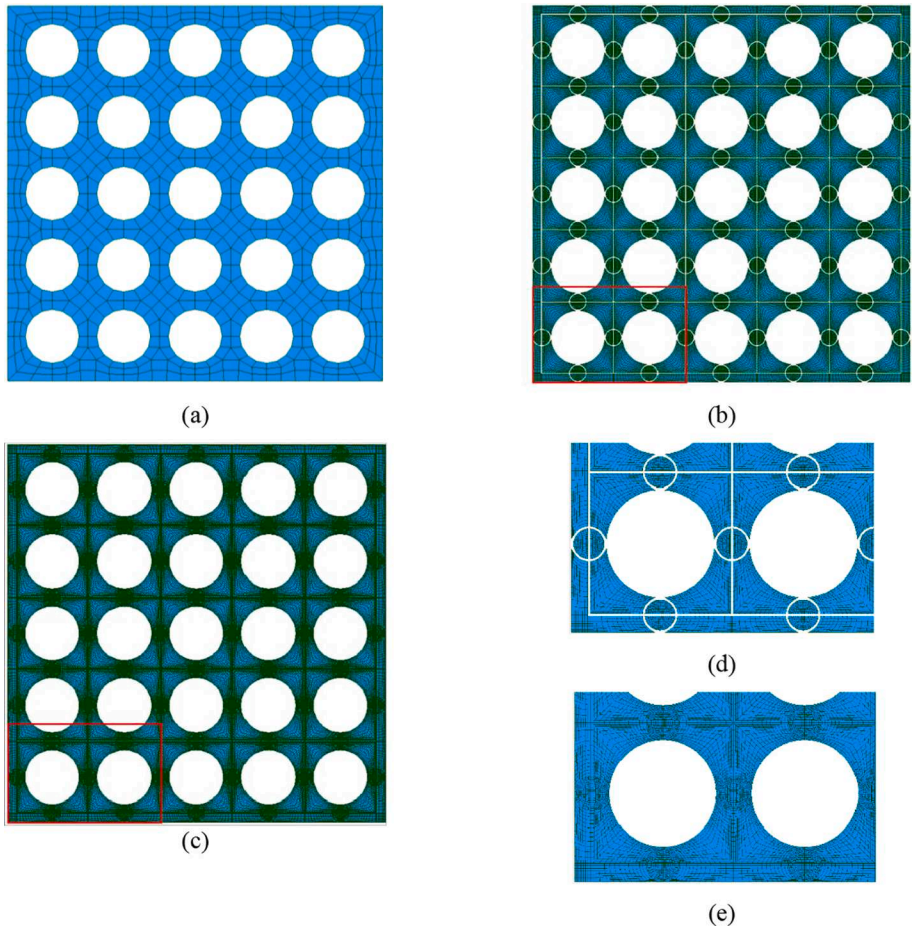

Fig. 8. Cross-sectional views of meshes used in the coupling system: (a) coarse-grid mesh for the SubChCFD baseline model, (b) spacer region of the CFD mesh for the resolved sub-model, (c) bare bundle region of the CFD mesh for the resolved sub-model, (d) local zooming in on Figure (b), (e) local zooming in on Figure (c).

model is 279 mm long (i.e. the one-span length), including a 241 mm downstream of the SSG, which covers all four elevations where circumferential wall temperature measurements are available. These elevations are z = –875 mm, z = –945 mm, z = –1015 mm and z = –1050 mm. The main part is extended by another 120 mm (approximately $12D_h$) in the upstream of the SSG to allow a certain distance between the coupling interface and the SSG, resulting in a longer domain than one grid span. Feedback from the fine-mesh domain to the coarse-mesh domain (two-way coupling) is deactivated in this extended transition section to avoid the flow development in the resolved model influencing the coarse-mesh model.

3.3.4. The overall domain arrangement

Fig. 7 is a schematic showing the final spatial arrangement of the computational domains in the modelling system. The coarse-grid model covers the entire length of the heated section with all 13 SSGs accounted for using embedded porous media models. The resolved sub-model covers mostly the first span of the test section where high fidelity experimental measurements for rod wall temperatures were performed.

3.4. Mesh system

Fig. 8 shows the cross-sectional views of the meshes used in the modelling system. It can be seen in Fig. 8(a) that the coarse-grid mesh used for the SubChCFD baseline model is generated based on mesh scheme 1 (Liu et al., 2019) and the resulting mesh size is 1.37 million cells. The mesh is the same for the bare bundle and the spacer gird regions, as the embedding porous media method does not require a separate mesh for the porous media sub-domains.

The CFD mesh used for the resolved sub-model is block-structured and contains purely hexahedral cells. Fig. 8(b) shows the cross-sectional view of the CFD mesh at the spacer region. The mesh is suitably refined near the surfaces of the grid straps to capture the wall effects therein. Such a mesh pattern extends in both axial directions to the regions without spacer grid to ensure a conformal transition across the interfaces. This is beneficial to the overall numerical accuracy of the simulation, but to some extent, results in an increase in cell density for those regions. The mesh is laterally periodic and magnified views of some representative structures are presented in Fig. 8(d) and (e) to shown more details. It can be seen in Fig. 8(d) that geometrical simplifications have been made to the regions where the SSG is in contact with the rods and the casing walls. The contact 'points' (from a 2-D cross-sectional perspective) are replaces with contact 'lines' to avoid the sharp angles on the two sides so that it is easier to ensure a high quality local mesh. In the axial direction, the mesh is refined in the vicinity of the SSG, especially in the downstream region, to capture the complex flow features in the wake. Finally, the mesh size for the resolved sub-model is 28.9 million cells.

3.5. Turbulence models

A two-equation eddy viscosity turbulence model, the k-ω SST model (Menter, 1994), is used in conjunction with a two-scale friction velocity wall function (EDF R&D, 2019) in the resolved sub-model to model turbulence. The same turbulence model is used in the coarse-grid SubChCFD baseline model to simplify the data exchange of turbulence quantities between the coupled models.

3.6. Boundary conditions

3.6.1. The coarse-grid SubChCFD model

For the coarse-grid baseline model, a recycling method is used, as described in Section 3.3.1, to derive the boundary condition for the inlet and an outflow boundary condition is used for the outlet. The solid walls of the rods and bundle casing are treated using a standard SubChCFD approach, where the wall friction factor is calculated using the following correlation (Todreas and Kazimi, 1990),

$$f = \left[a + b_1 \left(\frac{P}{D_h} - 1 \right) + b_2 \left(\frac{P}{D_h} - 1 \right)^2 \right] \Big/ Re^n \tag{14}$$

where P is the pitch of the square rod array (for edge or corner subchannels, P is equal to the rod dimeter plus the gap between the rod and the bundle wall), D_h is the subchannel hydraulic diameter, Re is the Reynolds number based on D_h and the subchannel bulk velocity, a, b_1, b_2 and n are constants, the values of which for different types of subchannels are given in Table 4.

Constant heat fluxes are imposed on the rod walls over the heated length based on the values given in Table 3 and the rest of the solid walls are assumed to be adiabatic.

Table 4
Parameters in the friction factor correlation for square-lattice rod bundles.

Subchannel type	a	b_1	b_2	n
Interior (laminar)	35.55	263.7	−190.2	1
Edge (laminar)	44.40	256.7	−267.6	1
Corner (laminar)	58.83	160.7	−203.5	1
Interior (turbulent)	0.1339	0.09059	−0.09926	0.18
Edge (turbulent)	0.143	0.04199	−0.04428	0.18
Corner (turbulent)	0.1452	0.02681	−0.03411	0.18

3.6.2. The resolved CFD sub-model

There are basically two types of boundaries in the resolved fine-mesh domain, namely, the actual physical boundaries and the coupling interfaces. All solid walls are actual physical boundaries and have non-slip conditions applied. The boundaries through which the flow enters and leaves the domain are coupling interfaces, and the boundary conditions for them are updated based on the coarse-grid results at each time step during the simulation. Dirichlet type boundary conditions are used for all variables except pressure at these coupling interfaces. They can be derived using equations of similar forms as Eq. (11). In this study, a new method has been developed to derive the boundary conditions for the inlet interface to improve the quality of the simulation as detailed in Section 3.7.

3.7. Improvements of the coupling methodology

In reality, the flow is expected to have fully developed before reaching the SSG in the target span, as it has actually passed through over 10 grid spans. Although the computational domain of the resolved sub-model has been extended by about $12D_h$ at the inlet, it is still not likely to be long enough for the boundary layer to fully develop. A simple solution is to further extend the domain to ensure the simulation results of the region of interest are independent of the location of the inlet boundary. However, this will result in a significant increase in the overall computing cost. Alternatively, a methodology is developed herein for the treatment of the boundary conditions at coupling interfaces (particularly the inlet interface in the present case) to reduce the boundary error without further increase in domain size. Details are as follows:

- The coarse-grid velocity and temperature are not directly mapped to the fine mesh to derive the inlet boundary conditions for the resolved sub-model. Instead, they are averaged over subchannels to produce corresponding bulk quantities, which are passed to the fine mesh.
- Empirical correlations are then used to produce well-developed flow and temperature profiles for each of the subchannels at the inlet boundary of the fine-mesh domain. Such profiles are further corrected to satisfy the conservation of mass and energy across the entire coupling interfaces.
- Fully-developed boundary profiles for the turbulence quantities (namely k and ω in this study) are also generated using relevant empirical correlations.

The empirical correlations used and a detailed procedure for implementation of the above methodology can be found in Section A1 of the Appendix.

3.8. Numerical simulation

A pressure-based steady-state solver is used for both of the coupled models. SubChCFD with the embedded porous models was first performed for the coarse-grid domain without coupling with the resolved

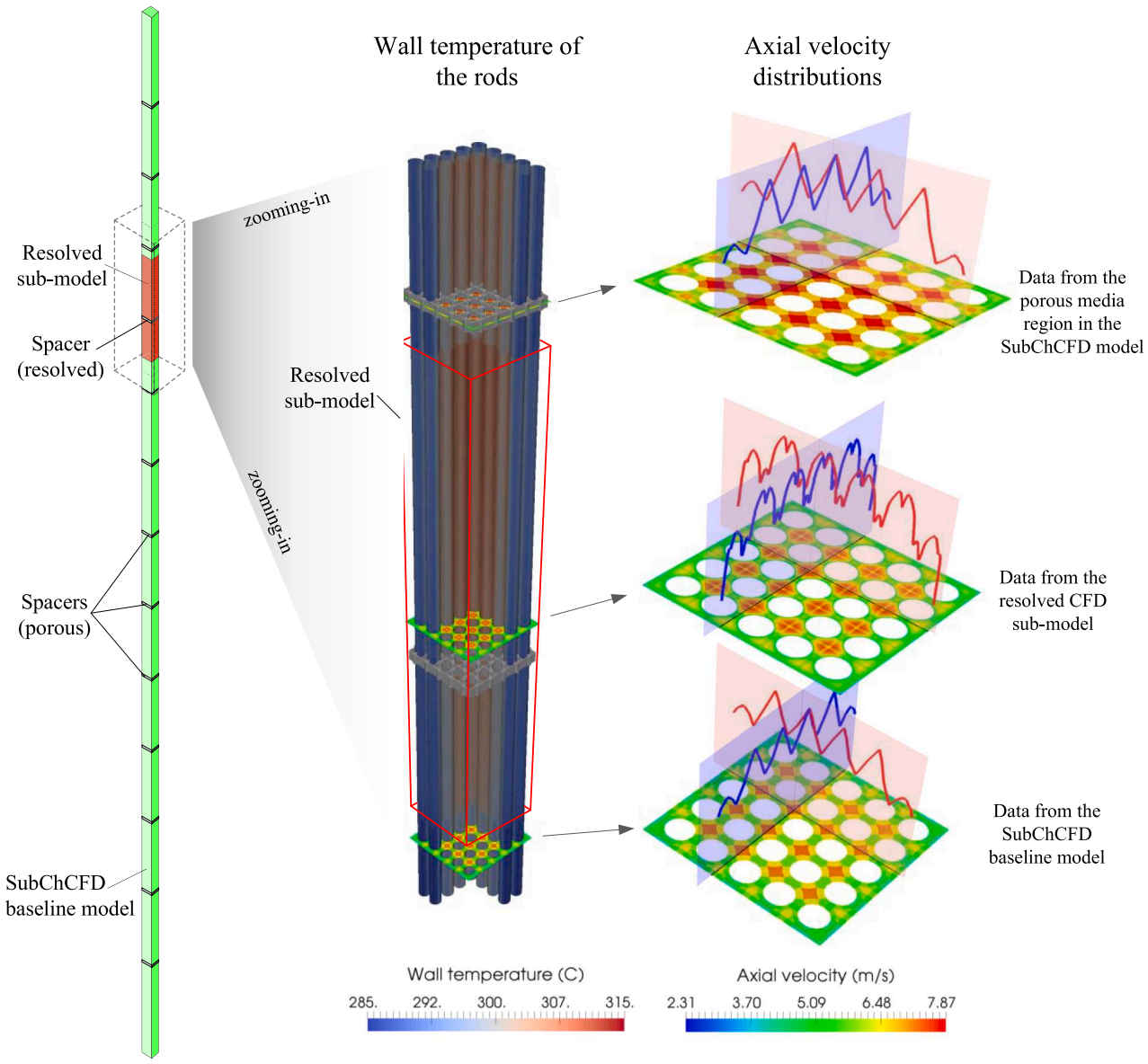

Fig. 9. Overall flow pattern predicted by the coupled model system.

CFD to gain some initial insights to the flow and provide a starting point for the coupled simulation so as to accelerate the convergence of the latter. The coupled simulation was then performed on a High Performance Computing (HPC) cluster using a total of 256 Central Processing Unit (CPU) cores. To achieve the best parallelised performance, CPU cores were allocated to the coupled models based on the ratio of their mesh sizes used. Consequently, 12 and 244 cores were allocated to the coarse-grid model and the resolved sub-model, respectively. Convergence was reached within 6 h (wall-clock time), which is expected to be much shorter than that required in a typical CFD simulation for the full span of the rod bundle (the computing time needed is estimated to be up to 60 h for a same number of CPU cores used).

4. Results and discussion

Before going into a detailed discussion of the simulation results, an overall picture of the flow predicted by the coupled model system is shown first in Fig. 9. It can be seen on the left of the figure that the resolved sub-model (in red) occupies a fairly small part of the entire geometry of the SubChCFD model system (in green) where the locations of the SSG spacers are also indicated. A magnification of the most interested region in the model system (i.e. the section enclosed in the dashed box) is shown in the rest of the figure, where some details of the predicted rod wall temperature and axial velocity distributions at some representative elevations are also presented.

4.1. Flow field

Fig. 10(a) and (b) show the spatial evolutions of the axial subchannel bulk velocity and pressure of an interior subchannel (highlighted in red) along the axial direction, respectively. In addition to the results of the coupled simulation (baseline + porous + resolved CFD), the SubChCFD results of an uncoupled simulation (baseline + porous model) are also plotted for comparison.

It can be seen in Fig. 10(a) that the subchannel bulk velocity gradually increases towards the outlet of the domain as the fluid is heated up and expanding due to the density decrease. Velocity spikes appear due to the reduction in area of the flow passage when the flow passes through the SSGs. Such a phenomenon is correctly captured by the use of the embedded porous media model in SubChCFD, as it is evidenced that the pattern and height of the velocity spike predicted by SubChCFD (with/without the coupled simulation) agrees well with that of the resolved

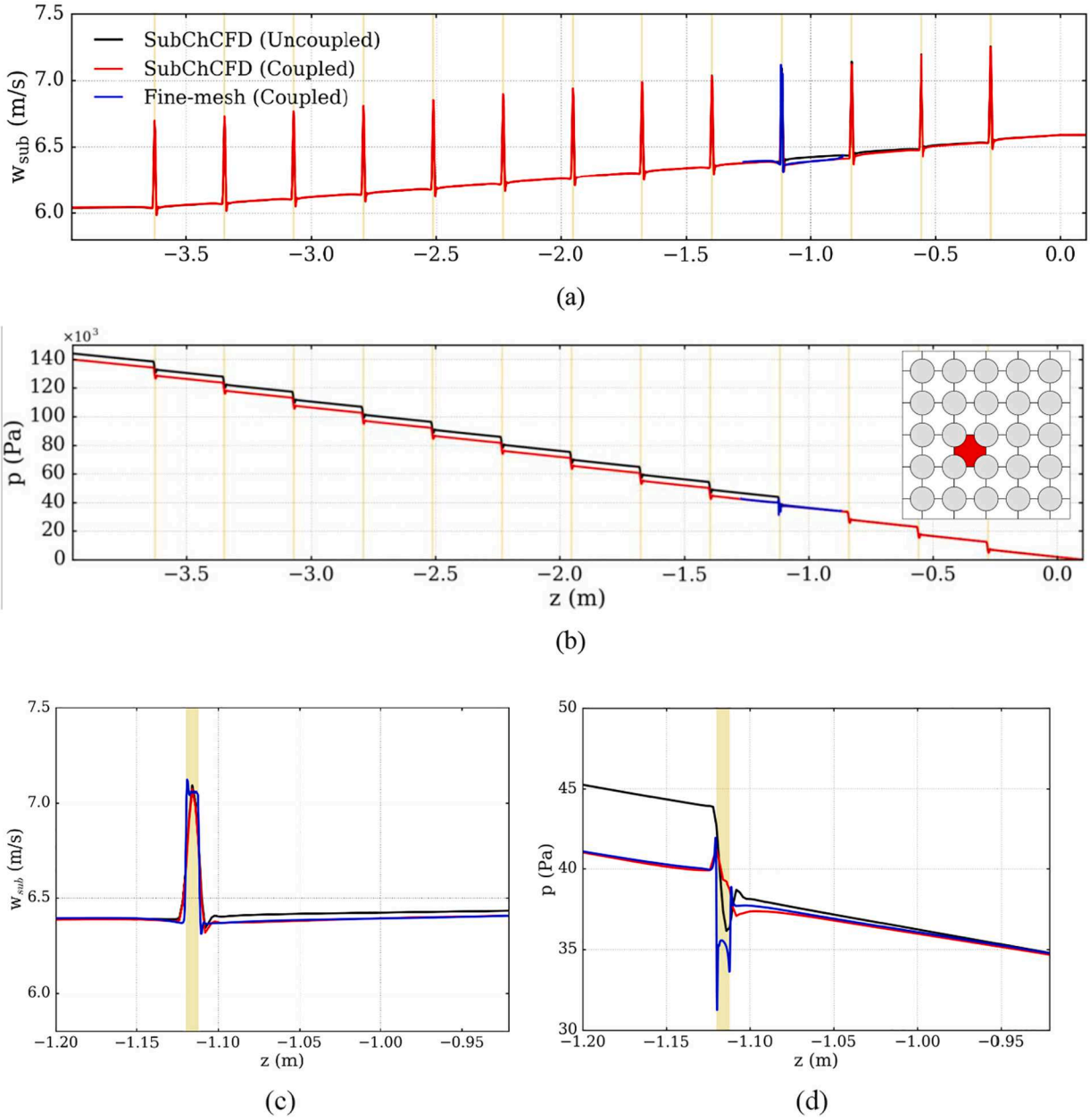

Fig. 10. Axial evolution of the flow at an interior subchannel: (a) subchannel bulk velocity, (b) pressure, (c) subchannel bulk velocity of the target span, (d) pressure of the target span.

sub-model where the SSG in the target span is explicitly resolved. It can be noted in Fig. 10(c) that the axial bulk velocity of the highlighted subchannel predicted by SubChCFD in the coupled simulation is slightly lower than that of the uncoupled simulation in the target span downstream of the SSG due to momentum correction through the two-way coupling. It is also worth noting that such a difference diminishes in the far downstream.

The overall pressure drop predicted in the coupled simulation is about 3.4% (5,000 Pa) lower than that in the uncoupled SubChCFD simulation. Such a difference originates, as shown in Fig. 10(b), in the grid span where coupling is located. For ease of analysis, the grid-span pressure drop can be divided into two components, that is, the frictional loss due to bare bundle and the form loss due to the addition of the spacer grid. In uncoupled SubChCFD, prediction of the two relies completely on empiricism through Eqs. (6), (14) and Table 4, and Eq. (13), respectively. In the coupled simulation, however, the empiricism is replaced by RANS CFD in the region of coupling. It can be seen in Fig. 10(d) that the coupled simulation agrees with the uncoupled SubChCFD in terms of the prediction in frictional loss but gives a much lower prediction of the form loss than that of the latter. This is somewhat consistent with what was observed in the Round Robin benchmarking exercise on an isothermal MANIVEL case where most of the investigated RANS models under-predicted the grid span pressure loss by 25 – 45% and the error was considered to be mainly due to the under-prediction of the form loss across the SSG (EPRI, 2014).

Fig. 11 shows a detailed comparison of the predicted grid span pressure drop between the present study and a number of CFD results produced using full-span-domain simulations in the Round Robin benchmarking exercise. These CFD simulations cover a variety of RANS turbulence models, wall treatments, mesh sizes and CFD packages used. Details can be found in Table 5.

The SSG is designed to be small and simple, but its effects on the flow are still expected to be significant. The axial velocity profile is expected to be highly distorted when the flow passes the SSGs. This phenomenon

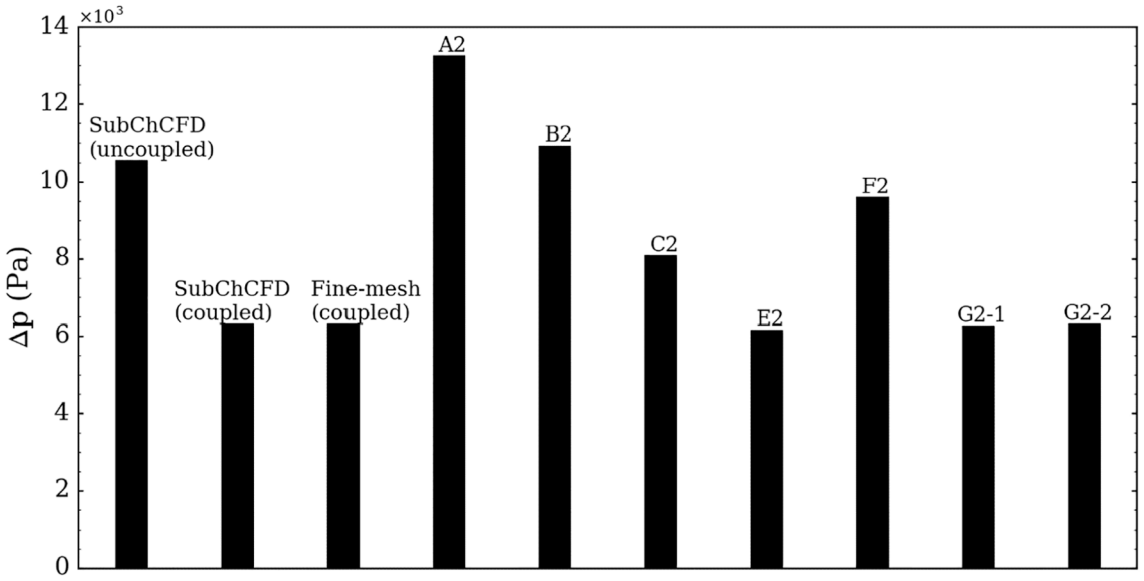

Fig. 11. Comparison of grid span pressure drop between the present simulation and some RANS CFD results in the Round Robin Benchmarking exercise.

Table 5
Detailed information of the selected full-span-domain CFD simulations in the Round Robin benchmarking exercise.

CFD Simulation	CFD package	Mesh size per grid span	Turbulence model	Wall treatment	CHT
A2	ANSYS Fluent	11 million (hybrid)	Steady RANS, k-ω SST	Enhanced wall treatment (EWT-ω)	Yes
B2	STAR-CCM+	35 million (hexa, trim)	Steady RANS, Modified quadratic k-ε	High y^+ treatment	No
C2	STAR-CCM+	22 million (hexa, trim)	Steady RANS, Modified quadratic k-ε	High y^+ treatment	Yes
E2	STAR-CCM+	7.6 million (hexa)	Steady RANS, Realizable k-ε	Two-layer all y^+ wall treatment	No
F2	STAR-CCM+	32 million (hexa, trim)	Steady RANS, Low-Reynolds-number k-ε	All y^+ wall treatment	Yes
G2-1	Code_Saturne	12.1 million (hexa)	Steady RANS, SSG RSM, SGDH	One-velocity-scale wall function	No
G2-2	Code_Saturne	12.1 million (hexa)	Steady RANS, SSG RSM, GGDH (Cθ = 0.15)	One-velocity-scale wall function	No

cannot be captured by a SubChCFD simulation by definition. One of the aims of coupling SubChCFD with a resolved sub-model is to capture some details of the grid effects on the flow downstream. Unfortunately, there are no measured velocity data available to directly assess the simulation results, as LDV measurements were not performed in the OMEGA experiments. Considering that the SSG rod bundle used in the MANIVEL facility is the same as that used in the current OMEGA case simulated herein, the velocity data of an isothermal case in the MANIVEL experiment are used as a base for comparison.

Fig. 12 shows the cross-sectional locations of the experimental data used, including two horizontal lines (Line 1 & Line 2) and two vertical

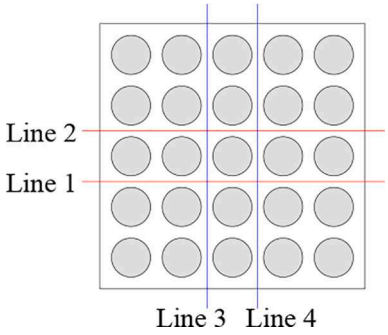

Fig. 12. Selected lateral locations of the measured mean axial velocity for assessment of the numerical simulations.

lines (Line 3 & Line 4). Since the flow is expected to be symmetric about the centrelines, experimental data are averaged over the pair of lines of the same orientation. Data at four different axial elevations downstream of the SSG in the target span are compared with the simulation results, including z-z_G = 35 mm, z-z_G = 50 mm, z-z_G = 100 mm and z-z_G = 160 mm (z_G represents the axial location of the downstream edge of the target SSG).

To make suitable comparisons, the velocities from simulations are normalised using the cross-sectional average values at each corresponding elevation, whilst the experimental measured data are normalised using the average inlet velocity in the isothermal case used. Considering the symmetry of the geometry and the flow, the simulation results are plotted only for Line 2.

Fig. 13 shows comparisons of the axial velocity profiles for the aforementioned four elevations. The two sets of experimental data for lines of different orientations are plotted separately and they are found to be in good agreement with each other. The coarse-grid results derived through an uncoupled SubChCFD simulation are also presented in addition to the coupled simulation results. It can be seen that the distortion to the axial velocity profile caused by the SSG is captured as expected by the resolved sub-model in the coupled simulation, although the peak values in the edge subchannel are under-predicted by around 10% for most of the elevations investigated. This may be due to a combination of the turbulence model used and the discrepancy of flow conditions between the OMEGA case simulated and the MANIVEL isothermal case used to provide the experimental data. But in any case,

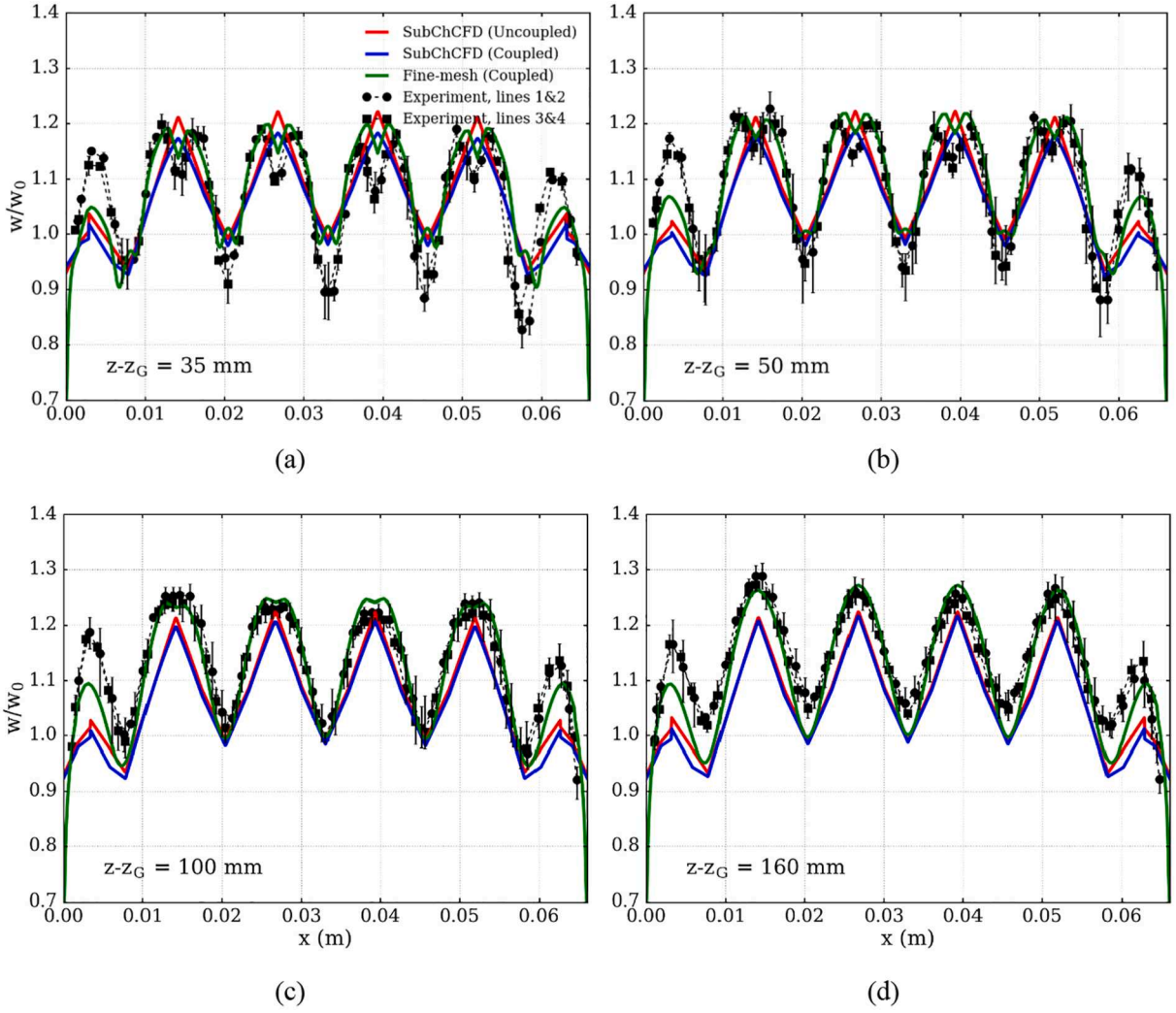

Fig. 13. Comparison of the mean axial velocity profiles normalized by corresponding bulk velocities along Line 2 at different elevations: the experimental data are plotted separately for Lines 1&2 and 3&4 (Note: the elevations are based on the MANIVEL isothermal experiment shown in Fig. 4).

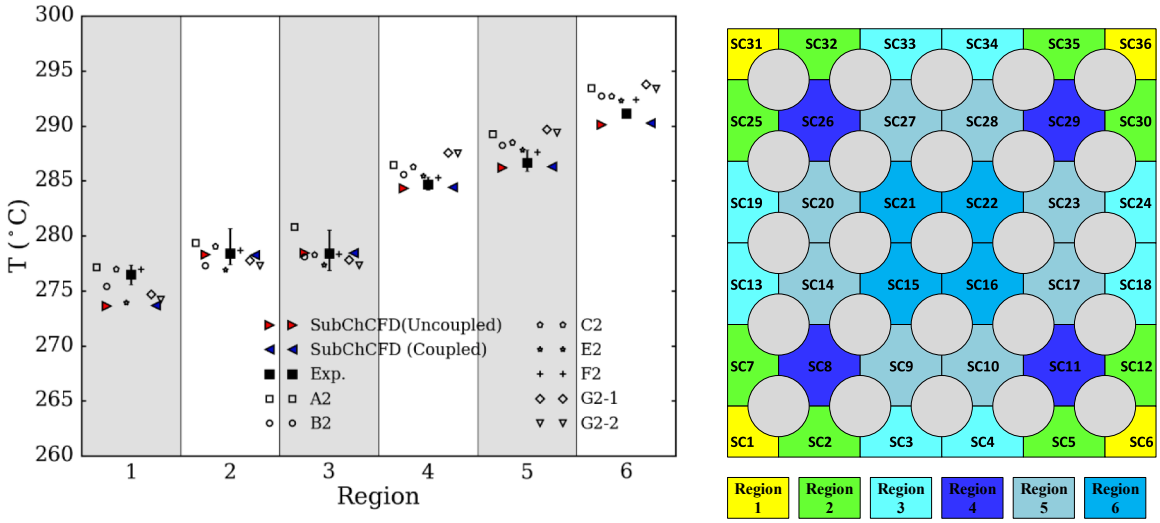

Fig. 14. Comparison of the region-averaged subchannel centre temperature at the EOHL.

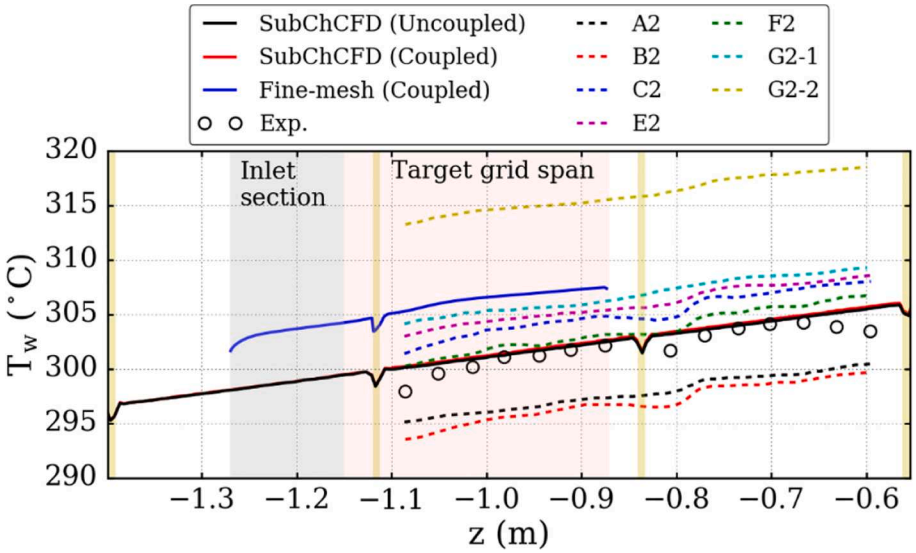

Fig. 15. Comparison of the axial evolutions of the circumferentially averaged rod wall outer-surface temperature over the central rod.

the fine-mesh results are a huge improvement over the coarse-grid counterparts which naturally do not capture any of the details mentioned above. Additionally, the two-way coupling seems to provide some noticeable 'improvements' to the coarse-grid results especially at the near-downstream elevations, in that the velocity peaks at the subchannel centres are slightly lowered. However, these improvements are small and may not be considered as a definitive conclusion.

4.2. Thermal field

4.2.1. Subchannel centre fluid temperature at the EOHL

Subchannel centre fluid temperatures were measured at the EOHL in the OMEGA experiments, so they can be directly used to assess the current simulation results. Since the resolved sub-model in the coupled simulation does not cover the measurement plane at the EOHL, only the coarse-grid results of the SubChCFD models are compared with the experiment. Fig. 14 shows the region-averaged subchannel centre temperatures at the EOHL for six different T/H types of subchannels that are indicated in different colours. It can be seen that the present simulation results agree well with the experiment measurements for most of the regions. The biggest disagreement happens at the corner subchannels where the temperature is under-predicted by around 3 °C. Despite this, the predictions of SubChCFD is better than those of most of the CFD models shown in Table 5.

It should be pointed out that no direct thermal coupling is used between the coupled models in the current simulation. In other words, the improvement for the coarse-grid temperature field is achieved through momentum corrections rather than being directly based on the fine-mesh temperature result. Feedback to the coarse-gird temperature field may further improve the results but is not included in the present study. Since the effect of momentum correction in the overlapping region does not propagate that far downstream (see Fig. 10), it is not surprising that there is almost no difference observed between the uncoupled and coupled SubChCFD results of the subchannel centre fluid temperatures at the EOHL.

4.2.2. Rod wall outer-surface temperature

A key target variable to assess the quality of the numerical simulation in this study is the rod wall outer-surface temperature. In the NESTOR-OMEGA experiment, the rod wall outer-surface temperature was calculated from the heating power and the measured rod wall inner-surface temperature based on the assumption of 1-D (radial) conductive heat transfer in the solids. In addition to the (calculated) experimental data, the results of the CFD models shown in Table 5 are also used for comparison. It should be noted that some of the CFD simulations also took Conjugate Heat Transfer (CHT) in to account.

In the coupled simulation, the rod wall outer-surface temperature for the target grid span is available in both the fine-mesh and the coarse-mesh results. The former is obtained in a standard way through the wall function used. The approach used in the SubChCFD model is described below. This is calculated based on a local reference fluid temperature (T_{ref}) and the subchannel Nusselt number (Nu) using the following relation:

$$T_w = T_{ref} - \frac{\dot{q} D_h}{\lambda \mathrm{Nu}} \tag{15}$$

where $\dot{q}$ is the local wall heat flux, λ is the thermal conductivity of the fluid. The subchannel Nusselt number is calculated using the Nusselt number for a circular pipe with a correction factor (Todreas and Kazimi, 1990):

$$\mathrm{Nu} = \psi (\mathrm{Nu}_\infty)_{c.t.} \tag{16}$$

where $\psi = 1 + 0.9120 Re^{-0.1} Pr^{0.4} (1 - 2.0043 e^{-B})$, $B = D_h/D$, and $(\mathrm{Nu}_\infty)_{\mathrm{c.t.}}$ is calculated using the Dittus-Boelter correlation (Dittus and Boelter, 1985):

$$(\mathrm{Nu}_\infty)_{c.t.} = \begin{cases} 0.023 Re^{0.8} Pr^{0.4} & \text{when the fluid is heated} \\ 0.023 Re^{0.8} Pr^{0.3} & \text{when the fluid is cooled} \end{cases} \tag{17}$$

Simulation results are first presented in the form of circumferentially averaged values. Fig. 15 shows a comparison of the axial evolution of the average rod wall outer-surface temperature in the target span. Here, the fine-mesh result in the inlet transition section is also included to show that the flow and the thermal boundary layers have already well developed before entering the target region and hence demonstrating the effectiveness of using the empirical correlations for the inlet boundary conditions of the fine-mesh domain. Detailed discussion about this can be found in Section A2 of the Appendix.

Interestingly, the coarse-mesh results (in the uncoupled and the coupled simulation) agree better with the experimental data than the fine-mesh result does in terms of temperature magnitude. They are even better than all the full-span CFD results presented. This is because SubChCFD incorporates well-validated and application-specific empirical correlations, which are sometimes found to be more accurate than resolved CFD. It is, however, worth noting that the coarse-mesh results do not show a convex shape as most of the full-span CFD results do in the

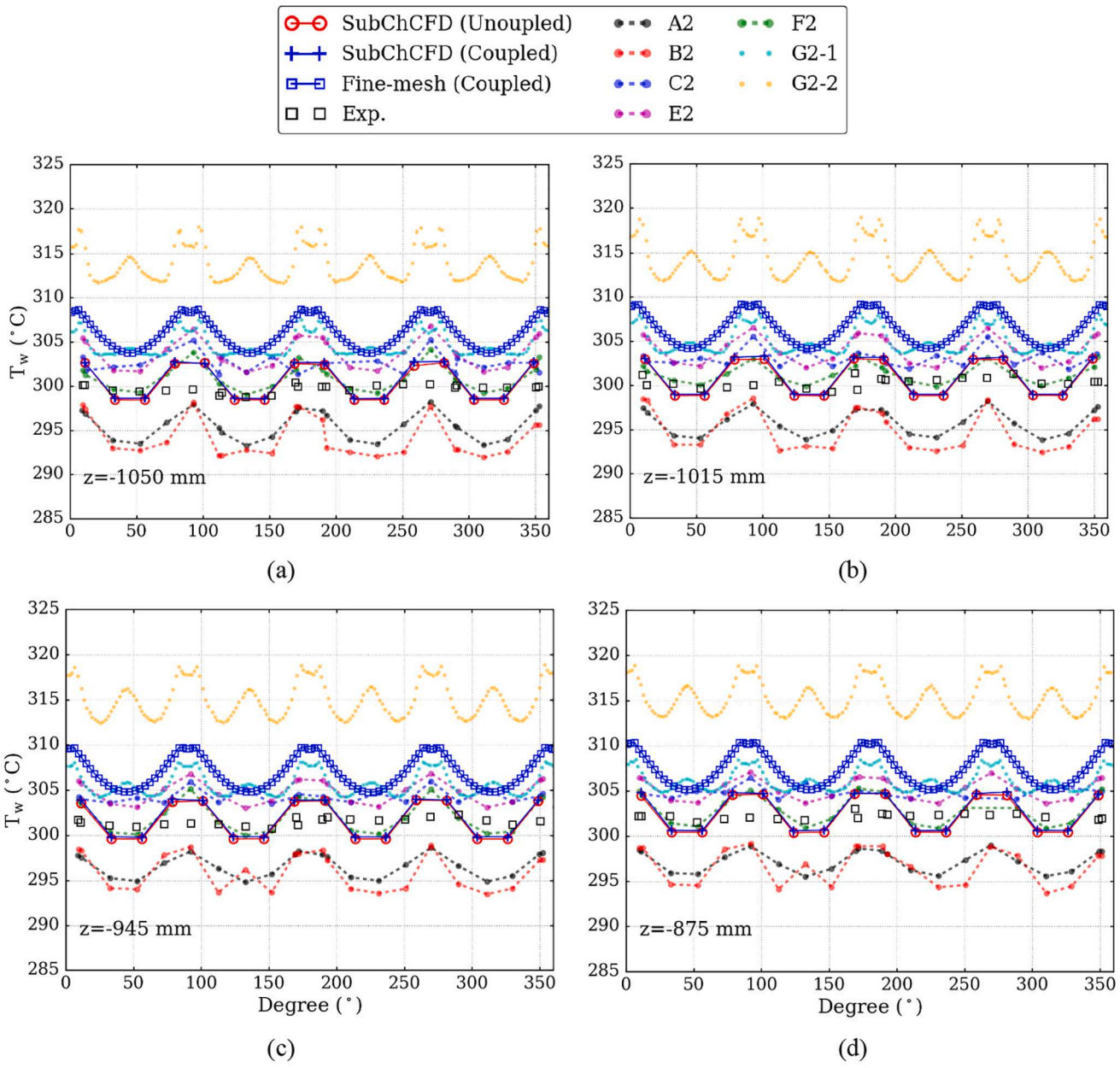

Fig. 16. Comparison of the circumferential distributions of the rod wall outer-surface temperature over the central rod at the four elevations shown in Fig. 6.

target grid span, although the feature is not significant. This is reasonable as (by definition) the coarse-grid model is not expected to resolve the detailed effects of the SSG on the flow and heat transfer downstream. Conversely, the fine-mesh result of the coupled simulation agrees well with most of the full-span CFD results as well as the experimental data in this regard, even though the overall magnitude of the wall temperature is over-predicted. It has been discussed in the report of the Round Robin benchmarking exercise (EPRI, 2014) that such an over prediction happened in all CFD simulations (except A2 and B2 in which a wall roughness was used), which may be due to the potential inaccuracy of the thermal boundary conditions of the rod walls calculated based on the 1-D heat conduction assumption. It can be noted that the most accurate predictions are observed in the cases where the CHT is taken into account (Case C2 and F2).

Fig. 16 compares the detailed circumferential distributions of the rod wall outer-surface temperature over the central rod at the four elevations for experimental measurements depicted in Fig. 6. Despite an over-prediction in magnitude, the fine-mesh results of the coupled simulation are consistent with most of the full-span CFD results (especially those produced using isotropic turbulence models) in terms of circumferential variations. A maximum of about 5 °C wall temperature variation along the circumferential direction of the rod is predicted. However, this is not the case observed in the experimental measured data which show a rather flat shape instead. It was argued in (EPRI, 2014) that the experiment results did not show a clear and consistent pattern and this may be caused by coarse measurement intervals, experimental errors and determination biases.

The circumferential variations of the rod wall outer-surface temperature predicted by the coarse-grid model are highly dependent on how the reference temperature in Eq. (15) is selected. In the current simulation, the temperature of the wall adjacent mesh cell is selected as the reference, leading to very similar predictions of the wall temperature distribution to those of resolved CFD approaches (see Fig. 16). It should also be noted that, similar to the situation observed for the average values in Fig. 15, the circumferential distribution of the rod wall outer-surface temperature predicted by the coarse-grid model in the coupled

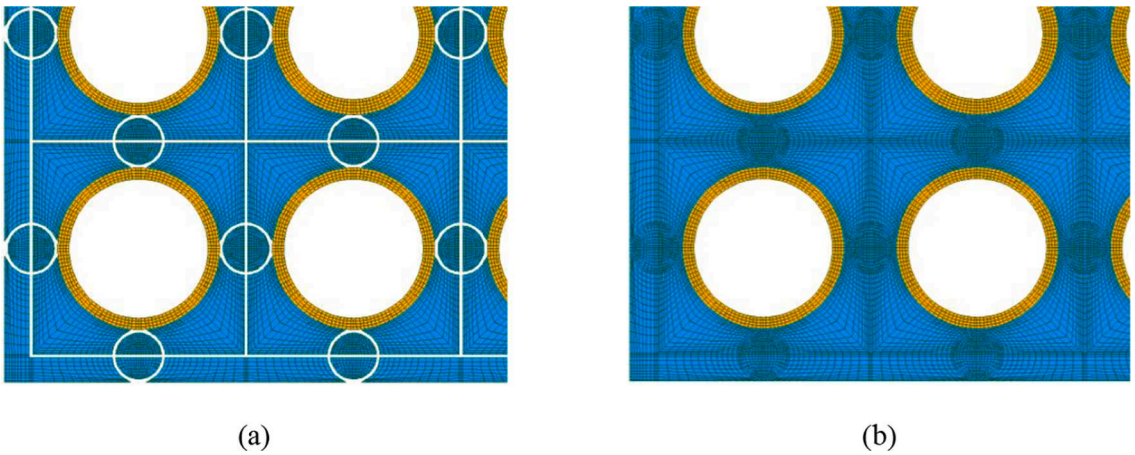

Fig. 17. Cross-sectional views of the mesh used for the resolved sub-model with solid heat conduction taken into account: (a) spacer region, (b) bare bundle region.

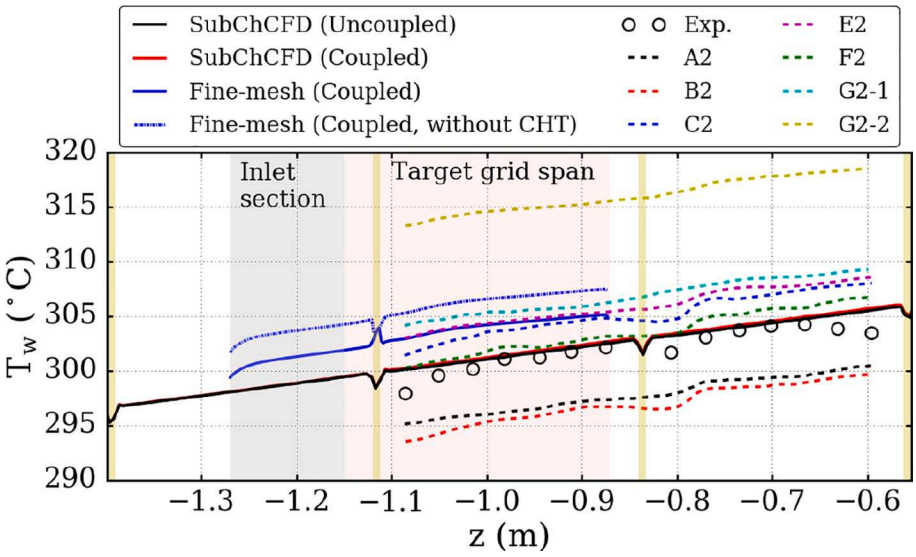

Fig. 18. Comparison of the axial evolutions of the circumferentially averaged rod wall outer-surface temperature over the central rod: CHT is considered in the resolved sub-model in the coupled simulation.

and the uncoupled simulations almost coincide with each other, indicating that the thermal correction due to the two-way coupling is very small.

4.3. Considering CHT in the resolved sub-model

CHT can be directly taken into account in the resolved sub-model without special adjustments to the current coupling framework. One of the most significant changes made to the resolved sub-model is to create a mesh for the solid zones where heat conduction is to be considered. Fig. 17 shows the cross-sectional views of some representative parts of the mesh. It can be seen that the solid walls of the 9 inner and the16 peripheral rods are meshed using 5 and 4 layers of cells in the radial direction, respectively. The circumferential divisions in the solid mesh are consistent with that in the adjacent fluid mesh to ensure conformal interfaces between the two. For simplicity, heat conduction inside the SSG (not expected to have significant effects) is not considered, so it is excluded from the computational domain. The total mesh size (including both the fluid and the solid meshes) increased to 34.4 million cells (28.9 million cells for the fluid and 5.5 million cells for the solid).

In the coupled simulation, the governing equations for the solid and the fluid zones in the resolved sub-model are handled in a single CFD instance taking advantage of the 'internal coupling' functionality of Code_Saturne. Adiabatic boundary conditions are used for the rod wall inner-surfaces and volumetric energy sources based on the actual heating power given in Table 3 are imposed uniformly to the corresponding tube rods over the heated length. Constant solid physical properties given in Table 2 are used in the solution of the heat conduction equation for the solid.

Fig. 18 shows the axial evolution of the circumferentially averaged rod wall outer-surface temperature over the central rod obtained in the new simulation. As expected, the coarse-grid results are almost the same as that of the previous simulation. However, the result of the resolved sub-model obtained in the new simulation is improved compared with the previous one where the CHT is not taken into account, although an over-prediction is still observed. As can be seen in Fig. 18, the over-prediction of the wall temperature in the new simulation is about 3 °C, whilst the value is about 5 °C in the previous one where CHT is not considered. This is consistent with what was reported in the Round Robin benchmarking exercise that CFD simulations with CHT supposed to give better predictions. It is worth noting that a small temperature peak is predicted by the resolved sub-model near the SSG in the target span. This may be due to the sudden change of the T/H condition of the

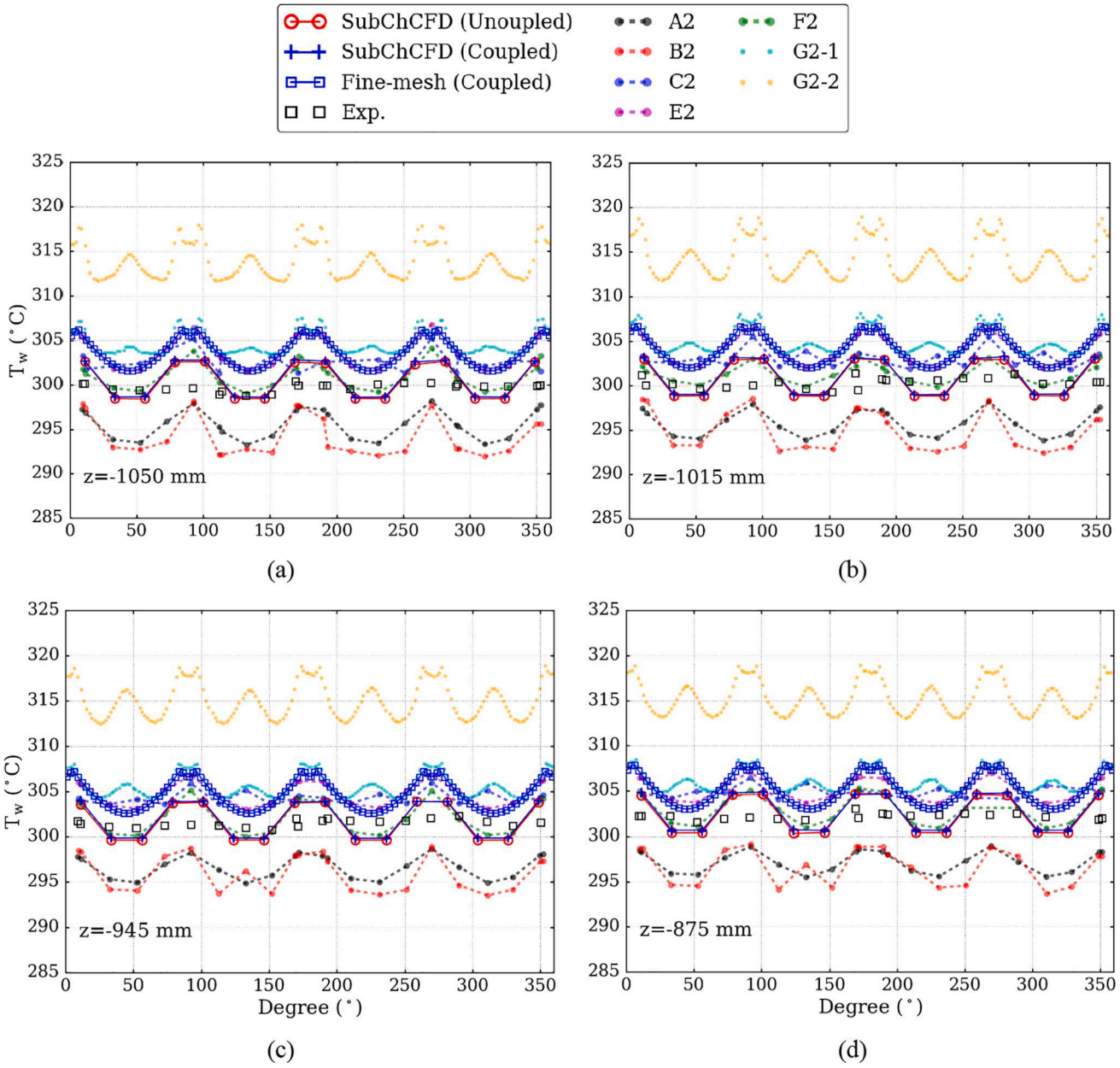

Fig. 19. Comparison of the circumferential distributions of the rod wall outer-surface temperature over the central rod at the four elevations shown in Fig. 6: CHT is considered in the resolved sub-model in the coupled simulation.

fluid when it passes the SSG. Such a peak does not appear in the CFD results of the Round Robin benchmarking exercise, as they are averaged at actual measurement locations which do not coincide with the SSG. Moreover, the predicted wall temperature peak here is in an opposite direction to that of the previous simulation. In the previous model, the wall surface area where the rod and the SSG are in contact are excluded from the fluid-domain boundaries, resulting in a slight reduction in total heat flux to the fluid in the spacer region, and this may account for the opposite prediction of the wall temperature peak.

Fig. 19 shows circumferential distributions of the rod wall outer-surface temperature over the central rod for the new simulation results. Again, the coarse-grid results are almost the same compared with the previous ones. The main difference in the new simulation results happens in the fine-mesh model where the overall magnitude of the wall temperature predicted is reduced by about 2 °C for each of the elevations investigated, but meanwhile the shape of the temperature distribution does not change significantly. It is a little surprising that the circumferential variation of the wall temperature is not smeared more significantly by the heat conduction inside the solid. Despite this, the result agrees well with that of a similar benchmarking CFD simulation with CHT (F2) in terms of the circumferential variation, in which an isotropic turbulence model (a low Reynolds number k-ε model) was used.

5. Conclusions

A 5 m 5 × 5 rod bundle with Simple Support Grids (SSGs) in the NESTOR-OMEGA experiment is used to demonstrate the multi-scaling simulation capability of SubChCFD in handling complex flow and heat transfer problems in large reactor core structures. A body-fitted coarse-grid mesh that covers the full length of the rod bundle is created based on the bare bundle geometry for the SubChCFD baseline model. The SSGs are modelled using the embedded porous media method to account for the reduction in area of the flow passages and the resultant pressure

drop. A resolved sub-model covering a particular grid span of interest is coupled with the coarse-grid model to explicitly resolve the detailed effects of the SSG on the flow downstream.

A new method has been proposed herein to improve the treatment of the interfacing boundary conditions in the coupling. First, the resolved sub-model is extended by $12D_h$ at the inlet to create a developing zone, where feedback from resolved to coarse-mesh model is switched off. Then, to accelerate flow development in this region, empirical correlations are used to obtain the inlet boundary conditions for the fine-mesh domain based on the bulk quantities from the coarse-mesh model. As a result, quasi-fully-developed inlet profiles for flow, temperature and turbulence quantities are obtained by the end of this developing zone and the axial length required for the flow to fully develop is reduced.

A two-equation eddy viscosity turbulence model, the k-ω SST model, is used for both of the coupled models to simplify the data exchange for turbulence quantities in the coupling. A two-scale friction velocity wall function is used in the resolved sub-model. The meshes used for the coupled coarse-grid and the fine-mesh models are 1.4 million cells and 28.9 million cells (increasing to 34.4 million cells when Conjugate Heat Transfer (CHT) is considered), respectively. The simulation was performed using 256 CPU cores on a HPC cluster, and a maximum 6-hour simulation turn-around time was achieved.

The simulation results are first compared with data of the NESTOR-MANIVEL isothermal experiments for the flow field, although the flow conditions are not exactly the same. With normalisation using the respective bulk velocities, the comparisons show that the axial evolution of the axial velocity profile in the target grid span is reasonably well captured by the resolved sub-model in the coupled simulation in comparison with the experimental data.

A key variable to assess the quality of the numerical simulation is the rod wall outer-surface temperature. Comparisons are made for the circumferentially averaged values over the central rod between the simulation results and the experimental data as well as a number of CFD results of the Round Robin benchmarking exercise. It is shown that the coarse-grid result agrees very well with the experimental data in terms of the overall temperature variations, but it does not capture some details of the axial evolutions as expected. In contrast, the resolved sub-model captures the variations correctly as most of the reference CFD simulations do, but over-predicts the temperature magnitude by about 5 °C. In a subsequent simulation with CHT considered, the over-prediction is reduced by 40%.

In addition, the resolved sub-model of the coupled simulation predicts very similar patterns of the circumferential variation of the rod wall outer-surface temperature to most of the full-span CFD simulations in the Round Robin benchmarking exercise (especially those with similar turbulence models). However, the amplitude of the wall temperature variation predicted is higher than that observed in the experiment (although this may be due to some uncertainties in the experimental measurements). Such a trend does not change significantly in the simulation with CHT considered, but the predicted overall wall temperature magnitude is much closer to the experiment.

To summarise, SubChCFD coupled with resolved-CFD and porous media model offers significant capability and good flexibility in representing the overall behaviour as well as resolving selected local flow features for a large flow/thermal system with complex internal structures. It is also noted that the predictions from a resolved CFD sub-model within SubChCFD are still limited in their accuracy (when compared with experimental data) by the inherent uncertainties and limitations in the CFD modelling approach used. For example, the limitations on the applicability of different RANS turbulence models to specific types of flow apply equally to these sub-models. Similarly, the success of the porous modelling approach depends on the suitability of, for example, user defined loss coefficients. It may further noted that SubChCFD incorporates well-validated and application-specific empirical correlations that are sometimes found to give better quantitative predictions than resolved CFD. Therefore, the SubChCFD tool offers the potential to achieve predictions that align more closely with experimental data than resolved CFD in some cases, as well as offering the large reduction in computational expense.

CRediT authorship contribution statement

B. Liu: Data curation, Formal analysis, Investigation, Methodology, Software, Writing – original draft. **S. He:** Conceptualization, Formal analysis, Funding acquisition, Investigation, Methodology, Supervision, Writing – review & editing. **C. Moulinec:** Software, Writing – review & editing. **J. Uribe:** Software.

Declaration of Competing Interest

The authors declare that they have no known competing financial interests or personal relationships that could have appeared to influence the work reported in this paper.

Acknowledgements

The present work was carried out as part of the R&D Program for Digital Reactor Design sponsored by the Department of Business, Energy and Industry Strategies (BEIS) of the UK (TRN 1659/10/2018). We appreciate the fruitful discussions with the project team members and are especially grateful for the useful feedbacks provided by C. Howlett and R. Underhill of Frazer-Nash Consultancy. The authors would also like to acknowledge the support received through EPSRC's Collaborative Computational Project (CCP) for Nuclear Thermal Hydraulics (No. EP/T026685/1).

Appendix A. Supplementary data

Supplementary data to this article can be found online at https://doi.org/10.1016/j.nucengdes.2022.111793.

References

Class, A.G., Viellieber, M.O., Batta, A., Fax, T., 2011. Coarse-Grid-CFD for pressure loss evaluation in rod bundles, in: Proceedings of ICAPP 2011. Nice, France, pp. 1773–1780.

Dittus, W., Boelter, L.M.K., 1985. Heat Transfer in Automobile Radiators of the Tubular Type. Int. Commun. Heat Mass Transf. 12, 3–22. https://doi.org/10.1021/acs.jproteome.6b00648.

EDF R&D, 2019. Code_Saturne version 6.0.0 practical user's guide.

EPRI, 2015. Computational Fluid Dynamics Benchmark of High Fidelity Rod Bundle Experiments Industry Round Robin Phase 2 -Rod Bundle with Mixing Vane Grids. Palo Alto, CA.

EPRI, 2014. Computational Fluid Dynamics Benchmark of High Fidelity Rod Bundle Experiments Industry Round Robin Phase 1 - Rod bundle with simple supporting grids. Palo Alto, CA.

Fiorina, C., Clifford, I., Aufiero, M., Mikityuk, K., 2015. GeN-Foam: A novel OpenFOAM® based multi-physics solver for 2D/3D transient analysis of nuclear reactors. Nucl. Eng. Des. 294, 24–37. https://doi.org/10.1016/j.nucengdes.2015.05.035.

Fournier, Y., Bonelle, J., Moulinec, C., Shang, Z., Sunderland, A.G., Uribe, J.C., 2011. Optimizing Code_Saturne computations on Petascale systems. Comput. Fluids 45, 103–108. https://doi.org/10.1016/j.compfluid.2011.01.028.

Gerschenfeld, A., Gorsse, Y., Fauchet, G., 2019. Development of a polyhedral staggered mesh scheme application to subchannel and CFD SFR thermal-hydraulics. 18th Int. Top. Meet. Nucl. React. Therm. Hydraul. NURETH 2019, 3329–3342.

Hanna, B.N., Dinh, N.T., Youngblood, R.W., Bolotnov, I.A., 2020. Machine-learning based error prediction approach for coarse-grid Computational Fluid Dynamics (CG-CFD). Prog. Nucl. Energy 118, 103140. https://doi.org/10.1016/j.pnucene.2019.103140.

Hu, R., Fanning, T.H., 2013. A momentum source model for wire-wrapped rod bundles - Concept, validation, and application. Nucl. Eng. Des. 262, 371–389. https://doi.org/10.1016/j.nucengdes.2013.04.026.

Liu, B., He, S., Moulinec, C., Uribe, J., 2021a. A Coupling Approach between Resolved and Coarse-grid Sub-channel CFD. Nucl. Eng. Des. 377, 111124. https://doi.org/10.1016/j.nucengdes.2021.111124.

Liu, B., He, S., Moulinec, C., Uribe, J., 2021b. Coupled porous media approaches in sub-channel CFD. Nucl. Eng. Des. 377, 111159. https://doi.org/10.1016/j.nucengdes.2021.111159.

Liu, B., He, S., Moulinec, C., Uribe, J., 2019. Sub-channel CFD for nuclear fuel bundles. Nucl. Eng. Des. 355, 110318. https://doi.org/10.1016/j.nucengdes.2019.110318.

Menter, F.R., 1994. Two-equation eddy-viscosity turbulence models for engineering applications. AIAA J. 32, 1598–1605. https://doi.org/10.2514/3.12149.

Mikuž, B., Roelofs, F., 2020. Low resolution modelling of mixing phenomena in PWR fuel assemblies. Nucl. Eng. Des. 360, 110504. https://doi.org/10.1016/j.nucengdes.2019.110504.

Rehme, K., 1973. Pressure drop correlations for fuel element spacers. Nucl. Technol. 17, 15–23. https://doi.org/10.13182/NT73-A31250.

Roelofs, F., Doolaard, H., 2017. Towards 3D CFD Models of PWR Fuel Assemblies at Reasonable Computational Costs, in: Proceedings of 17th International Topical Meeting on Nuclear Reactor Thermalhydraulics (NURETH-17). Xi'an.

Roelofs, F., Gopala, V.R., Chandra, L., Viellieber, M., Class, A., 2012. Simulating fuel assemblies with low resolution CFD approaches. Nucl. Eng. Des. 250, 548–559. https://doi.org/10.1016/j.nucengdes.2012.05.029.

Todreas, N.E., Kazimi, M.S., 1990. Nuclear Systems I: Thermal Hydraulic Fundamentals. Taylor & Francis.

Viellieber, M., Class, A.G., 2012. Anisotropic porosity formulation of the coarse-grid-CFD (CGCFD), in: Proceedings of the 2012 20th International Conference on Nuclear Engineering Collocated with the ASME 2012 Power Conference ICONE20-POWER2012. California, pp. 1–11.

Wells, D.M., Peturaud, P., Yagnik, S.K., 2015. Overview of CFD round robin benchmark of the high fidelity fuel rod bundle NESTOR experimental data, in: Proceedings of 16th International Topical Meeting on Nuclear Reactor Thermal Hydraulics. Chicago, pp. 627–639.

Yoon, S.J., Kim, S.B., Park, G.C., Yoon, H.Y., Cho, H.K., 2017. Application of Cupid for Subchannel-Scale Thermal-Hydraulic Analysis of Pressurized Water Reactor Core Under Single-Phase Conditions. Nucl. Eng. Technol. 50, 54–67. https://doi.org/10.1016/j.net.2017.09.008.

Yu, Y., Merzari, E., Obabko, A., Thomas, J., 2015. A porous medium model for predicting the duct wall temperature of sodium fast reactor fuel assembly. Nucl. Eng. Des. 295, 48–58. https://doi.org/10.1016/j.nucengdes.2015.09.020.